MICROTUBULE PATTERNING AND MANIPULATION USING ELECTROPHORESIS AND SELF-ASSEMBLED MONOLAYERS

A Dissertation

by

JOHN A. NOEL

Submitted to the Office of Graduate Studies of
Texas A&M University
in partial fulfillment of the requirements for the degree of

DOCTOR OF PHILOSOPHY

May 2009

Major Subject: Applied Physics

MICROTUBULE PATTERNING AND MANIPULATION USING ELECTROPHORESIS AND SELF-ASSEMBLED MONOLAYERS

A Dissertation

by

JOHN A. NOEL

Submitted to the Office of Graduate Studies of
Texas A&M University
in partial fulfillment of the requirements for the degree of

DOCTOR OF PHILOSOPHY

Approved by:

Chair of Committee,	Winfried Teizer
Committee Members,	Wayne Saslow
	Alexandre Kolomenski
	Wonmuk Hwang
Head of Department,	Edward Fry

May 2009

Major Subject: Applied Physics

ABSTRACT

Microtubule Patterning and Manipulation Using Electrophoresis and Self-Assembled Monolayers. (May 2009)

John A. Noel, B.S., Texas A&M University

Chair of Advisory Committee: Dr. Winfried Teizer

We developed new methods for controlling and studying microtubules (MTs) outside the complex workings of the living cell. Several surface treatments for preventing MT fouling on surfaces were analyzed and, for the first time, a self-assembled monolayer (SAM) was developed which prevented MT adsorption in the absence of passivating proteins. The morphology and thickness of the SAM was measured to determine the mechanism of formation and origin of the MT-resistant behavior. The SAM was integrated into electron beam lithography for patterning and manipulating MTs using electrophoresis. Reversible MT adsorption and patterning and alignment of single MTs were achieved. We characterized the mechanism for the MT migration under electric field with a focus on the electrodynamics of the flow cell and the forces acting on the MT, along with the time dependence of the process.

DEDICATION

To Granny Jeanette Thompson, our endless source of

kindness, wisdom and encouragement

ACKNOWLEDGEMENTS

I would like to thank my advisors, Dr. Winfried Teizer and Dr. Wonmuk Hwang for their guidance and dedication. Thanks also go to my labmates, especially Raj, Arlene, Kyongwan, Joel and Huachun for their helpful discussions. Finally, thanks to my mother and father for all of the solutions to life's problems, to my brothers for supplying the problems, to my in-laws for taking me as I am, and to my wife for her impatience and infinite love.

TABLE OF CONTENTS

CHAPTER Page

LIST OF FIGURES

FIGURE Page

LIST OF TABLES

NOMENCLATURE

ACS	American Chemical Society
AFM	atomic force microscopy
ARXPS	angle resolved x-ray photoelectron spectroscopy
BE	binding energy
DC	direct current
DI	deionized
DPN	dip-pen nanolithography
DNA	deoxyribonucleic acid
EAL	electron attenuation length
EBL	electron beam lithography
EGTA	ethylene glycol-bis(2-aminoethylether)-*N,N,N′,N′*-tetraacetic acid
GMPCPP	guanosine-5'-[(α,β)-methyleno]triphosphate
GTP	guanosine triphosphate
KE	kinetic energy
KOH	potassium hydroxide
MAPs	microtubule-associated proteins
MCP	microcontact printing
MeOH	methanol
MIBK	methyl isobutyl ketone
MPEOPS	2-[methoxypoly(ethyleneoxy)propyl]-trimethoxysilane

MT	microtubule
NEM	N-ethylmaleimide
PEG	poly(ethylene glycol)
PIPES	piperazine-N,N′-bis(2-ethanesulfonic acid)
PMMA	poly(methyl methacrylate)
SAM	self-assembled monolayer
XPS	x-ray photoelectron spectroscopy

CHAPTER I

INTRODUCTION

1.1 Overview

This project was initiated through a desire to harness the interesting phenomena observed in microtubule (MT) filaments for application in nanotechnology, and to further the understanding of the fundamental properties of MTs. Upon consideration of methods to approach these goals, two questions arise. First, in what ways is it possible to control these dynamic filaments outside of the cellular environment? Second, how may we apply advanced nanofabrication and microscopy techniques to study MTs?

In general, to control biomolecules in a cell free environment, two major issues must be addressed. The first is preventing undesirable adsorption, or fouling, and the second is immobilizing the target biomolecules. Of these two goals, the former must be addressed as a prerequisite to the latter as the fouling is often irreversible in the laboratory time frame and may dominate over targeted interactions at the micro or nanoscale. Initially, we determined that a suitable method for preventing fouling of MTs to synthetic surfaces was lacking. Thus, we quantitatively analyzed several methods including surface coatings, surfactants and hydrophilization. This included, in part, the development of a new method for preparing protein resistant self-assembled monolayers

---

This dissertation follows the style of *Nano Letters*.

(SAMs) where the key steps were: elevated temperature, extended formation time, and a relatively moist environment. The utility of these SAMs was tested by fabricating patterned gold microstructures directly on the SAM and demonstrating that the SAM retained its MT- resistant property after lithographic processing.

Having succeeded in preparing an effective MT resistant surface, the next step was to immobilize the MTs and direct MT motion in the cell-free environment. To achieve this, the MT-resistant SAM was integrated into the lithography procedure. The gold was used as a biocompatible surface that could attract and bind MTs through chemical functionalization and through electrophoretically induced adsorption. Using DC electrophoresis, we then demonstrated that MTs could be reversibly adsorbed to the gold structures and that it was possible to pattern and align these filaments on arbitrarily shaped gold templates. In addition, single MT adsorption and orientation was observed.

Several phenomena were observed during electrophoresis experiments, including a threshold potential below which no MT motion was seen, an exponential decay in the rate of MT adsorption while under constant potential, and an asymmetry in the MT migration velocity for MTs approaching the electrode versus those being repelled. The threshold potential required to achieve the deterministic motion of MTs was explained in the context of thermal forces that tend to randomize particle motion. Modeling of the electrophoresis setup as an electrolytic capacitor reproduces the decay in MT adsorption rate. Analysis of the drag forces acting on cylindrical rods near a surface as compared to the bulk explained the asymmetry in MT migration velocity.

To understand the MT resistant nature of the SAM within the context of the body of research concerning protein adsorption to nonfouling surfaces, we analyzed the SAM using atomic force microscopy, ellipsometry and x-ray photoelectron spectroscopy to determine the roughness, morphology and thickness of the film. The results indicated that the MT resistant SAM was of monolayer thickness, contained a high surface density of molecules, and presented flexible polymer chains at the solution-surface interface. Previous experimental findings and theoretical models on SAM passivation indicated that the latter two properties (high density and flexible polymer at interface) are likely responsible for the effective prevention of MT fouling, and that several steps in the SAM preparation protocol were critical to achieving the MT resistant state.

1.2 Microtubules, Kinesin and Nanotechnology

Microtubules are hollow cylindrical filaments 25 nm in diameter which self-assemble from the protein tubulin and serve many functions in plant and animal cells.[1] In nerve cell processes, which can be meters in length, MTs assemble into pathways along which double headed kinesins 'walk' to transport material (Figure 1.1a,b).[2] Smaller cells distribute material by diffusion, which is adequate for short distances but would require years to move intracellular cargo to the distal ends of nerve cells.[1,3] Microtubules also serve as load bearing and polarizing structures during cell locomotion and cell division.[4,5] In order for MTs to perform their many roles, they must be able to quickly disassemble and reassemble according to signals from the cell and environment; a

property termed ‘dynamic instability.’ Dynamic instability is regulated by the binding and hydrolysis of guanosine triphosphate (GTP) by tubulin.[6]

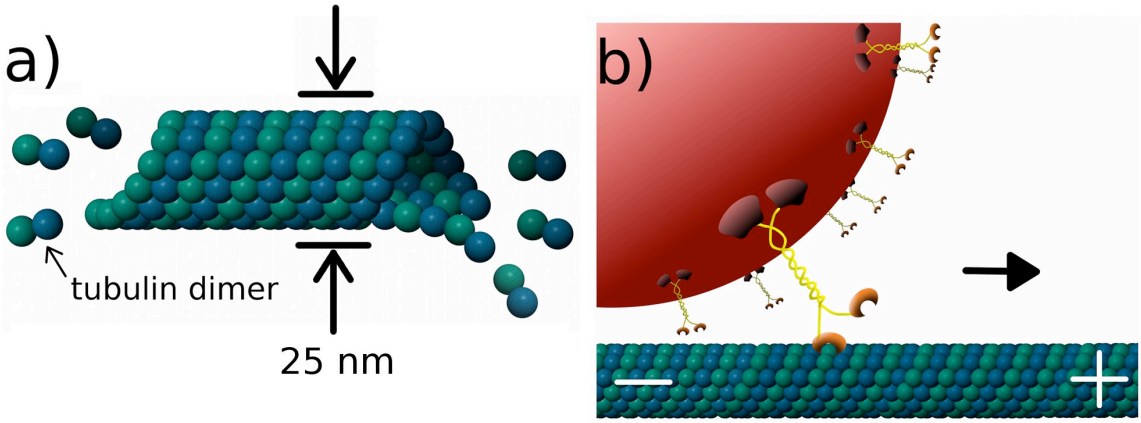

Figure 1.1 Microtubule and kinesin transport. (a) Cartoon of microtubule showing shape and polymerization through addition of tubulin dimers. (b) Cargo transport along microtubule by kinesin motor proteins (not to scale).

The ability to control microtubule orientation and dynamics in a cell free environment could lead to their use as nanoscale tracks for cargo carrying motor proteins. Guided self-assembly of microtubule-based structures may make possible hybrid assemblies that reconfigure based on minute electromagnetic or chemical signals, mimicking the cell.[7] Success in these areas will ultimately be met when one is able to control the stability, polarity, surface interactions, and bundling of MTs. For instance, MTs quickly depolymerize when the pH, ionic concentration or temperature stray from physiological norms; however taxol has been found to stabilize MTs under a broader range of conditions.[8] Many other compounds and microtubule associated proteins which modify MT behavior have been discovered. Just a few of these and their action are listed in Table 1.1.

Table 1.1 Modifiers of MT behavior.[9-16] Note: NEM is N-ethylmaleimide. GMPCPP is an analog of GTP, being guanosine monophosphate with two added nonhydrolyzable phosphate groups.

Taxol[a,b]	a. stabilizes against depolymerization
glycerol[c]	b. alters protofilament number
GMPCPP[a,b,c]	c. lowers critical concentration of tubulin
zinc[d]	d. 'unzips' MTs into sheets
γ-tubulin[e]	e. nucleates polar MT growth
NEM[f]	f. prevents polymerization at negative end of MT
tau[a,g]	g. regulates cargo transport on MTs

1.3 Motivation

Harnessing the dynamic functions of microtubules provides a method for building hybrid nanobio systems from the bottom up. Currently there are no well-developed methods for controlling MT organization and polymerization using engineered surfaces. MTs are a major structural component in cells and nerve fibers, and are essential for cell division, cell motility and vesicle transport. MTs are also a target for treatment of cancer and Alzheimer's.[17,18] The interest in MTs stems not only from the vital functions they perform in the cell but also their ability to act as nanoscale shuttles driven by motor proteins, as scaffolds for guided assembly of nanoparticles, and as a basis for synthesizing nerve-like systems.[17,19,20]

CHAPTER II

PREVENTING BIOFOULING OF MICROTUBULES USING SURFACE PASSIVATION

2.1 Introduction

2.1.1 Biofouling

Biofouling (or simply 'fouling' in this report) is the unwanted adsorption of biological materials on manmade surfaces, and occurs almost anywhere that water is in contact with these surfaces. Fouling is a major concern for maintenance of seagoing vessels because barnacles and other sea life can significantly increase drag and accelerate the deterioration of the hull.[21] This fouling is difficult to prevent and, over time, may require costly repairs or disable the vessel entirely. Fouling introduces similar problems in filtration systems for wastewater treatment and desalinization.[22] Implanted medical devices also risk becoming fouled by the immune response of the body, although some, such as stents, can be made of biodegradable materials to make use of this property.[23]

Fouling is initiated by nonspecific adhesion of proteins to the synthetic surface and may be followed by a buildup of additional layers of material.[21-23] Because of their small size, proteins can approach very close to the synthetic surfaces increasing the strength of electrostatic interactions.[24,25] Due to the variety of amino acid side chains present on a protein surface several types of molecular interactions with the substrate may occur, with hydrophobic and electrostatic being most dominant. The variety of

protein surface fouling mechanisms makes high quality passivation difficult, although there are several methods capable of reducing protein adsorption, the most common being poly(ethylene glycol) or carbohydrate surface modification, surfactant additives, and passivating protein layers.[26-28] Surfaces presenting poly(ethylene glycol) (PEG) (or poly(ethylene oxide)) are the most common because they block protein adsorption well and may be chemically crosslinked to gold, silicon, glass and other synthetic surfaces.[29-31] However, several challenges to improving PEG modification remain, specifically poor long-term stability, a dearth of simple chemical synthesis and crosslinking procedures, and reliable methods for patterning resistant surfaces.[32-38]

2.1.2 Preventing MT Fouling

At the time of this study, there were no publications that used PEG modification for the prevention of MT adsorption. Because MTs tend to adhere strongly to glass and silicon surfaces, the milk protein casein is frequently used for surface passivation.[19] However, passivation using PEG SAMs would have several advantages over casein. First, the hydrophobic interaction that binds caseins to the silica surface allows for exchange of casein with other proteins in solution and is considerably less stable than the covalent bonds of grafted organosilane SAMs. This increased stability, the variety of chemical modifications and the ability of organosilanes to form ordered, smooth surfaces makes them more suitable as substrates for lithographic process and protein patterning. Second, the mechanisms for preventing protein adsorption with grafted layers have been studied in much detail, providing several models through which one can analyze the interaction

between MTs and organosilane SAMs; this is discussed in the following chapter.[29] In contrast, the mechanism through which casein prevents protein adsorption is not well understood.[39] Bovine serum albumin, another commonly used passivating protein, suffers the same problems (exchange and stability) as casein and, in preliminary experiments in our lab, did not prevent MT adsorption on glass, silicon or gold surfaces.[40] Hydroxylation of glass and silicon by oxidizing agents, such as Piranha solution, create high surface hydrophilicity.[41,42] Surfactants are able to block protein adsorption when used as an additive to the protein containing solution or as a surface passivation prior to protein introduction.[43-45] Although substrate hydrophilization and surfactants show MT-resistant properties, they are not suitable for creating binary surfaces because they make poor substrates for micro and nanofabrication and, by their nature, it is difficult to geometrically restrict them on the surface.

Current techniques used for quantification of protein adsorption are: infrared and photoelectron spectroscopy, ellipsometry, quartz crystal microbalances, surface plasmon resonance, atomic force microscopy (AFM) and fluorescence microscopy.[26,30,46-52] Of these, all except fluorescence microscopy and AFM are bulk measurements that detect protein adsorption indirectly through alteration of an optical or electrical substrate signal. AFM and fluorescence microscopy locally image the surface, capturing spatial distribution and density of adsorbed proteins and can also give some information on protein conformation and orientation. Further, the high sensitivity of fluorescence detection allows measurement of protein surface concentration down to 0.14 ng/cm^2, much better than surface plasmon resonance, which can detect approximately 0.5 ng/cm^2

and ellipsometry, which is of limited use below 1% of a full protein monolayer.[42,53,54] Fluorescence microscopy is also ideal for detecting MT adsorption on SAMs because individual MTs can be imaged easily with a low background, made possible by high quality bandpass filtration of the emitted fluorescence.

2.2 Assaying Surface Passivation Methods for Preventing MT Fouling

2.2.1 Materials and Methods

2.2.1.1 Materials

SAMs were made using 2-[methoxypoly-(ethyleneoxy)propyl]-trimethoxysilane (MPEOPS), 95%, from Gelest, Inc. High purity, lyophilized bovine brain tubulin (unlabeled and rhodamine fluorophore labeled) was purchased from Cytoskeleton, Inc. A nonhydrolyzable guanosine nucleotide (GMPCPP) was used for MT polymerization (Jena Biosciences, GmbH). Triton-X 100, ethylene glycol-bis(2-aminoethylether)-*N,N,N′,N′*-tetraacetic acid (EGTA), glucose oxidase, peroxidase, glucose, 2-mercaptoethanol, Piperazine-N,N''-bis(2-ethanesulfonic acid) (PIPES), taxol, hydrogen peroxide (30%) and sulfuric acid (96%) were purchased from EMD Chemicals. Isopropanol, acetone, toluene and chlorobenzene were all ACS grade and obtained from EMD Chemicals. Polymethylmethacrylate (PMMA, MW 950K) was obtained from Brewer Scientific. Methylisobutylketone (MIBK, ACS grade) was obtained from Fisher Scientific. No.1 borosilicate glass coverslips (22 X 50 mm) were purchased from VWR.

Polished electronic grade p type <111> silicon wafers were purchased from Addison Engineering, Inc.

2.2.1.2 Microtubule Preparation

The following microtubule preparation procedure, adapted from the lab of Tim Mitchison at Harvard, was used for all surface passivation assays. Briefly, rhodamine labeled tubulin (50 μM) was mixed with unlabeled tubulin (50 μM) at a ratio of 1:2 in PIPES buffer (80mM Piperazine, 1mM $MgCl_2$, 1mM EGTA, pH 6.8 with KOH) containing 5% glycerol and 1μM GMPCPP. The tubulin was allowed to polymerize for 37ºC for 30 minutes then diluted to a concentration of 0.5 μ M in PIPES buffer supplemented with 20 μM taxol. Before each assay, oxygen scavenging cocktail (glucose 45 mg/mL, glucose oxidase 2 mg/mL, catalase 0.35 mg/mL, 2-mercaptoethanol 5 % v/v in PIPES buffer) was freshly prepared and added to the MTs to prevent depolymerization from fluorescence excitation. The final tubulin concentration used was 0.45 μM unless specified otherwise.

2.2.1.3 Assaying Passivation

We analyzed various surface treatments to find a passivation method which is highly effective at preventing MT adsorption and which would be compatible with lithographic methods. The level of nonspecific MT adsorption on glass and silicon substrates which have been treated with either hydroxylation, Triton-X 100 surfactant (Triton-X), a poly(ethylene glycol) SAM, or casein was measured using fluorescence microscopy. MT

adsorption to cleaned glass and silicon surfaces was used as a control. To assay passivation of sample surfaces, fluorescently labeled taxol stabilized MTs (approximately 45 nM tubulin concentration) were flushed into flow cells assembled by fixing the treated sample surface face down onto a cleaned a glass coverslip using double-sided tape (Figure 2.1). Solutions were pipetted into one end of the flow cell while a Kimwipe was used to wick the solution out of the other end. The typical volume of the flow cell was about 4 μL. In experiments that required displacement of one solution with another, we flushed in 40 μL of each additional solution to assure a complete volume exchange. Because each flow cell was assembled by the juxtaposition of a clean glass coverslip and a test surface, we were able to examine both surfaces concurrently. After allowing the MTs to adsorb for five minutes, the unattached MTs were flushed out with 40 μL PIPES buffer supplemented with an oxygen scavenging solution. The MT adsorption was observed at 60X magnification under a Nikon TE2000 microscope equipped for fluorescent imaging. The amount of MT adsorption was surveyed by capturing images of ten different regions distributed across each surface. Using NIS-Elements software (Nikon, Inc.), the total pixel area covered by MTs was tabulated. In each assay, the adsorption of MTs to the clean glass coverslip was monitored as a control in order to prevent errors arising from sample-to-sample variation in fluorescence intensity and MT concentration.

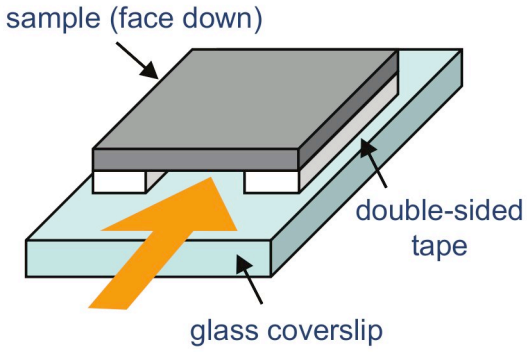

Figure 2.1 Flow cell for MT passivation experiments. Arrow shows direction of fluid injection.

2.2.1.4 Hydrophilization

Borosilicate glass coverslips are referred to here as 'glass' surfaces while electronic grade silicon wafers with a native oxide layer are referred to as 'silicon' surfaces. The standard cleaning procedure, as referred to in this work, consists of sonication of fresh substrates in acetone for five minutes followed by rinsing with isopropanol and drying with nitrogen gas. Glass substrates were made hydrophilic by hydroxylation with Piranha solution (hydrogen peroxide in sulfuric acid, 1:4, v/v). The substrates were first cleaned with acetone and isopropanol as described above and then immersed under fresh Piranha solution, which was hot due to the exothermic reaction from mixing, for ten minutes followed by rinsing with deionized water and drying with nitrogen gas. The substrates were then rinsed with 0.1M KOH for 10 seconds followed by a rinsing with DI water and drying under nitrogen.[41]

2.2.1.5 Casein Protein Passivation

Casein was used to passivate the surfaces according to standard motility assay protocols.[55] Briefly, a 'blocking' solution of 0.05 mg/mL casein in PIPES buffer was flushed into the flow chamber that was assembled as above using a cleaned silicon wafer as the sample surface. The casein was allowed to passivate the surfaces for 5 minutes and then the MT solution which has been supplemented with 0.2 mg/mL casein was flushed into the chamber and the remainder of the assay carried out as above.

2.2.1.6 Surfactant Treatment

Triton-X surfactant was used to passivate surfaces in the same way as casein. A blocking solution containing 0.05% v/v Triton-X in PIPES buffer was flushed into the flow chamber and left for 5 minutes. Triton-X at 0.05% was also added to the MTs before they were flushed into the chamber. The remainder of the assay was performed as above.

2.2.1.7 PEG SAM Preparation

For SAM preparation, the PEG-silane was mixed to 5% v/v in toluene and stirred for 1 minute. Silicon substrates, 8 to 10 pieces cut to approximately 1 cm x 1 cm, were cleaned with the standard procedure (in the hydrophilization section above), placed in the bottom of a 250 mL glass beaker and covered with 20 mL of the SAM solution. The beaker was placed in a ventilated oven at 75 °C for 21 hours. After removal from the oven, a viscous residue of PEG-silane covered the wafers and the bottom of the beaker.

The substrates were then rinsed vigorously with toluene, then rinsed with isopropanol and dried with nitrogen gas. Passivation assays were carried out as described above.

2.2.2 Results and Discussion

2.2.2.1 Passivation Assay

The results, reported in Figure 2.2 and Table 2.1, indicate that the SAM and casein passivate silicon surfaces extremely well. Triton-X and hydrophilization worked well on glass but not as well on silicon. It is generally accepted that hydrophilic surfaces exhibit reduced protein adhesion over charged and hydrophobic surfaces and Turner, et al., have shown that MTs in particular adsorb less readily to glass and silicon surfaces after treatment with Piranha and KOH.[41,42] Our results, however, showed that this treatment was not effective at preventing MT adsorption on silicon, resulting in 79% relative MT coverage as compared to 86% for clean silicon (Table 2.1). Hydrophilization was much more successful at passivating glass surfaces, reducing the overall value to 18%. The poor result for silicon was most likely due to an incomplete hydroxylation with this procedure.[56]

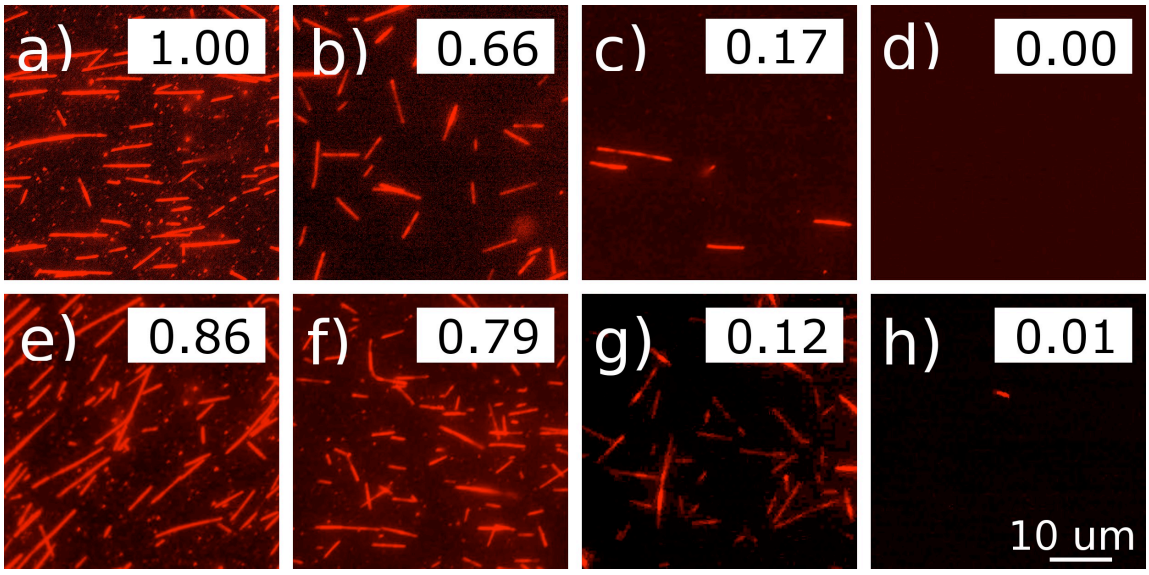

Figure 2.2. Sample images from passivation assay. Values given are area fouled by MTs (red filaments) relative to clean glass, which is scaled to 1.00. Top row of images show MT fouling on clean glass (a), hydrophilic glass (b), Triton-X treated glass (with Triton-X in solution) (c), and casein on glass (d). Bottom row shows fouling on silicon that is clean (e), hydrophilic (f), Triton-X treated (with Triton-X in solution) (g), and PEG-SAM coated (h). Details for each treatment are given in the text.

High purity surfactants have been successfully used to reduce protein adsorption on patterned surfaces.[43] Our results indicate that Triton-X was most successful when used to passivate the flow cell prior to MT injection in addition to being included in the MT solution at 0.05% v/v. Compared to the nonspecific adsorption on clean silicon substrates, this method was moderately successful in reducing MT adsorption, with area coverage of 66% of the value for clean glass. However, as with the hydrophilization, Triton-X was much more successful at reducing MT adsorption on glass substrates, resulting in 12% as compared to the clean glass.

Table 2.1 Passivation of silicon and glass to MT adsorption. Values reported as average area covered by MTs. The area MT coverage was scaled to the value for the clean glass substrate in each passivation assay, except for Triton-X where it was measured in a surfactant free solution of MTs. Error tabulated from standard deviation of MT coverage across all ten images captured for each assay. No MTs were detected on casein coated surfaces.

	clean	hydrophilic	Triton X	PEG SAM	casein
silicon	0.8620 ± 0.1423	0.7927 ± 0.1312	0.6589 ± 0.0909	0.0079 ± 0.0082	0
glass	1.0000 ± 0.3087	0.1772 ± 0.0776	0.1181 ± 0.0237	N/A	0

As expected, the MT adsorption to the casein-passivated surface was below the level of fluorescence detection. Casein is used in most cell-free MT studies because it passivates a variety of surfaces to MT adsorption including glass, silica, gold and SAMs. Interestingly, casein which has been subjected to lithographic resist coating and removal retains its function in kinesin motility assays.[57] Nevertheless, casein is not ideally suited as a substrate for lithographic patterning because of the intrinsic denaturing conditions such as vacuum and organic solvents and because the mechanism for casein passivation is not well understood.[58] Further, casein used in this way is nonspecifically adsorbed and may not be irreversibly bound, thus most protocols require free casein to be present in the solution.

PEG-silane SAMs have been shown to be quite stable and exceptionally resistant to protein fouling. Van den Heuvel, et al. successfully incorporated a PEG SAM onto engineered surfaces for rectifying MT-kinesin motility and studying MT docking to kinesin covered electrodes.[59,60] Because, in those reports, casein was used in addition to the SAM, we studied the ability of the SAM to resist MT adsorption in the absence of casein. The protocol used in the current work was adapted from Papra, et al.[61] The

results, presented in Table 2.1, indicate that this SAM is extremely resistant to MT adsorption, comparable to casein, with over 99% MTs blocked. These results were achieved without additional surface oxidation in Piranha prior to SAM formation and in the absence of hydrochloric acid in the SAM solution as outlined by Papra, et al. This SAM preparation method and the antifouling nature indicate that the SAM formation likely occurs through an initial condensation of the silane at the wafer surface with subsequent lateral crosslinking of adjacent silane molecules through Si-O-Si bonds, as noted elsewhere.[62] Our experiments indicate that SAMs prepared in this way are quite robust as they can be flushed clean, dried, sonicated in organic solvents, and reused without loss of nonfouling properties.

2.2.2.2 Comparison to Previous Studies on Protein Adsorption to SAMs

The degree of MT fouling we found is difficult to directly compare to the protein fouling in previous works due to variation in the analyzed proteins as well as the measurement techniques. However, it is useful to compare in at least a semi-quantitative manner the antifouling ability of the SAM in our work to previous studies that present absolute measurements on protein adsorption. Recent work by Clare, et al. and Unsworth et al., measured the fouling of several common proteins (avidin, fibrinogen and lysozyme) to methoxy terminated SAMs on silicon and were able to obtain adsorption as low as 0.14 ng/cm^2 and 10 ng/cm^2, respectively. The direct observation of MTs carried out for this study allows an estimation of the total adsorbed mass of tubulin for comparison. In Appendix A, we estimate the total tubulin mass measured in the passivation assay

experiments by calculating the MT length and estimating the number of tubulin dimers present. As a result, we found a value of 2.4×10^{7} ng/cm^2 (for the same data used to calculate the relative adsorption reported in Table 2.1), which is considerably larger than the values obtained in the previous studies. However, the value we report was obtained by assuming the entire mass of tubulin within the MT is fouled to the surface, while this is most likely not the case, which would put the actual value much lower than the estimate.

2.3 Conclusion

The passivation assay determined that, aside from casein passivation, the PEG SAM was the most effective at preventing MT adsorption. Hydrophilic glass and Triton-X were moderately successful at preventing adsorption. The robustness and versatility of the PEG SAM makes it the most promising for integration into devices for MT manipulation and patterning.

CHAPTER III

CHARACTERIZATION OF MT-RESISTANT SAMS

3.1 Background

The criteria for what may be called a 'SAM' are not well defined. A loose definition is a surface bound layer of amphiphilic polymers that condense from a solution or vapor phase with a preferred orientation. In this sense SAMs are similar to Langmuir-Blodgett layers, although SAMs are more strongly linked to the surface through chemisorption rather than physisorption.[63] Following their introduction to the surface science community in the 1980s, most SAMs have been formed from either an alkanethiol on Au or an organosilane on silicon oxide. Since that time the application of SAMs has grown tremendously due to the diversity of available tail groups which tailor the properties of synthetic surfaces.[64] PEG-silane SAMs were studied in this work because preliminary results with PEG thiol SAMs did not show adequate passivation against MT adsorption and because silane SAMs are more stable.[35] After achieving success in developing a SAM protocol for a reproducible and effective MT-resistant SAM, several questions arose. Why does the SAM block MT adsorption so well? What is special about this preparation procedure that reliably forms the MT-antifouling SAM while similar procedures do not? To answer these questions, we characterized the structure and morphology of the SAM and developed a likely scheme of formation within the context of previous studies.

Although surface functionalization by PEG for protein antifouling has become widely used, there are very few reports of SAMs formed directly from commercially available PEG-silanes in a one-step procedure, as in this work.[34] More often, additional steps must be taken, such as forming a precursor layer, to which PEG is then grafted, synthesizing a PEG-silane prior to assembly, or inducing SAM formation with a catalyst.[65-69] Further, trimethoxysilanes have only been studied relatively recently and less often than the more reactive trichlorosilanes.[29,61,66,70,71]

SAMs are commonly characterized by measuring wettability, surface density of SAM molecules, SAM thickness, nature of surface bonding, and topography. We characterized the SAM using ellipsometry, angle resolved X-ray photoelectron spectroscopy (ARXPS) and atomic force microscopy (AFM). These methods are able to determine the thickness, morphology and roughness of the SAM.[29,30,37,72]

3.2 Materials and Methods

3.2.1 Ellipsometry

Ellipsometry was carried out on a Nanofilm EP 3-SE ellipsometer on both the SAM coated wafer and the bare wafer with the native silicon oxide layer present. Ellipsometry for thickness measurement is based on the change in polarization of light as it reflects off of a surface with a transparent film. The light can be decomposed into components (parallel and perpendicular), and the ratio of the reflection coefficients of the parallel

polarized, r_p, and perpendicular polarized, r_s, components of light after reflection is given by:

$$\frac{r_p}{r_s} = \tan(\Psi)e^{i\Delta},$$

where Ψ is the amplitude ratio (normalized to the incident beam), Δ is the phase change between the incident and reflected signals, and the polarization is measured relative to the surface plane.[73] By convention, only the polarization of the electric field is considered, and we ignore the magnetic field.[73] The amplitude ratio and the phase change are functions of the refractive index and thickness. Thus, the thickness can be extracted from the values of Ψ and Δ by computer models. For the SAM, a fixed complex refractive index, $\tilde{n} = n + ik$ was ultimately used with the extinction coefficient, k, set to 0.[73] Using the vendor software, the ellipsometry data was fit to a simple three layer model (air, overlayer, substrate) under the assumption that both the SAM and the silicon oxide are thin, continuous, and transparent and have an index of refraction of 1.46.[73] This value for the index of refraction is correct within 3% and such small deviations in the real value for the index of refraction will have a miniscule effect on the calculated thickness.[70,74] Data was recorded at an angle of incidence of 54° relative to the surface plane. Because the SAM and native oxide are indistinguishable to the ellipsometer, they are modeled as a single overlayer. The thickness of the SAM is then calculated by subtracting the thickness of the oxide from the total overlayer thickness.

3.2.2 Angle Resolved X-ray Photoelectron Spectroscopy (ARXPS)

X-ray photoelectron spectroscopy (XPS) was used to analyze the compare the surface composition of unmodified silicon to PEG SAM modified silicon. Angle resolved XPS measurements were made to determine the thickness of the SAM (Figure 3.1). The physical principle of XPS is the excitation by x-rays (photons) of core electrons (1*s*, 2*s*, 2*p*, etc.) of the target material. The atom absorbs the photons, ionizing the atom, which then emits photoelectrons. The binding energy (BE), the energy required to remove the electron from the atom is specific to the energy shell and element from which it was emitted. An electron energy analyzer measures the frequency of and kinetic energy (KE) of emitted electrons. The BE of the electrons is then determined by conservation of energy:

$$BE = h\nu - KE,$$

where $h\nu$ is the energy of the x-rays of frequency ν (h is Planck's constant).[75] Due to interaction of the photoelectrons with the atoms, only those originating from within about 10 nm from the surface of the material reach the analyzer. However, this effect allows determination of the thickness of thin overlayers by measuring the emission at glancing angles (Figure 3.1).

PEG SAMs were prepared as described in the passivation assay section. XPS measurements were carried out using a Kratos Axis Ultra Photoelectron Spectrometer with a monochromated Al K_α (1486.6 eV) source. All measurements were made at pressures lower than $2x10^{-7}$ torr.

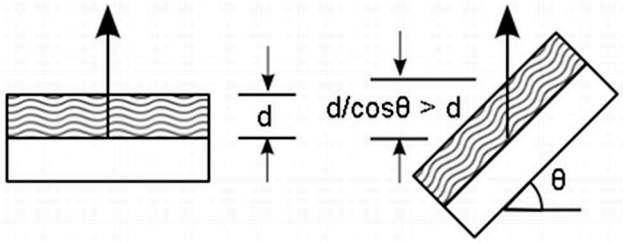

Figure 3.1. Thickness measurement using ARXPS. Film of thickness *d* shown. An arrow shows the direction at which photoelectrons are collected. As angle θ increases, the photoelectrons emitted from the substrate must travel farther through the film.

In order to verify the grafting of the SAM onto the substrates, three areas on each sample were analyzed with survey scans over a range of binding energy from 0 to1400 eV. High resolution scans of O 1s, C 1s and Si 2p regions were also made. The analyzer was oriented at an angle of $\theta = 0°$ from the surface normal for these measurements. Data including peak intensity and elemental composition was analyzed using the vendor software. Angle resolved XPS measurements were made by varying θ from 0° to 75°.[72]

3.2.3 Atomic Force Microscopy

Atomic force microscopy (Veeco CP II) analysis was carried out to determine the surface roughness and morphology of the SAM and silicon substrates. AFM is based on the measurement of the deflection of a cantilever as it is rastered over the sample surface. An electric feedback circuit analyzes the amount of the deflection and continuously adjusts either the height (constant force) or the force (constant height) by using piezoelectric adjustment. For tapping mode AFM, the cantilever is driven to oscillate at near its resonant frequency so that during rastering, the tip of the cantilever

samples the surface intermittently without continuously contacting the surface, allowing for lower deflection forces to be measured.

Tapping mode AFM was used in ambient air at frequencies ranging from 70-90 kHz. Cantilevers were antimony-doped silicon with a spring constant of 15 N/m and nominal tip diameter of 8 nm. We scanned a minimum of four 1×1 μm^2 regions on two samples for both the bare silicon and the SAM. The average of the root-mean-square roughness, R_{RMS}, was determined. The reliability of the AFM results was tested by scanning the same region in both the x and y direction and by determining the range of height values. The latter test was done to verify smoothness by looking at the maxima of deviation from the mean height values for each sample.

3.3 Results

3.3.1 Ellipsometry

From the ellipsometry data, the SAM and native oxide thickness were determined to be 3.26 ± 0.66 nm and 1.75 ± 0.05 nm, respectively, where the error is reported as the standard deviation across the three different measurement regions. We repeated the fitting with slightly different refractive index values and determined this had a negligible effect on the calculated thickness values.

3.3.2 X-ray Photoelectron Spectroscopy

Only carbon, silicon, and oxygen were detected from survey scans of the bare and SAM coated substrates (Figure 3.2). The peak intensity of the SAM modified surface showed a significant increase in the C 1*s* region and a moderate increase in the O 1*s* region as compared to the unmodified wafer (Figure 3.2b-c). The Si 2*p* intensity remained relatively constant (Figure 3.2a). These results confirm that the silane layer is present on the surface, as shown by the attenuation of the background signal from the Si substrate and the existence of significant amount of carbon after SAM formation.

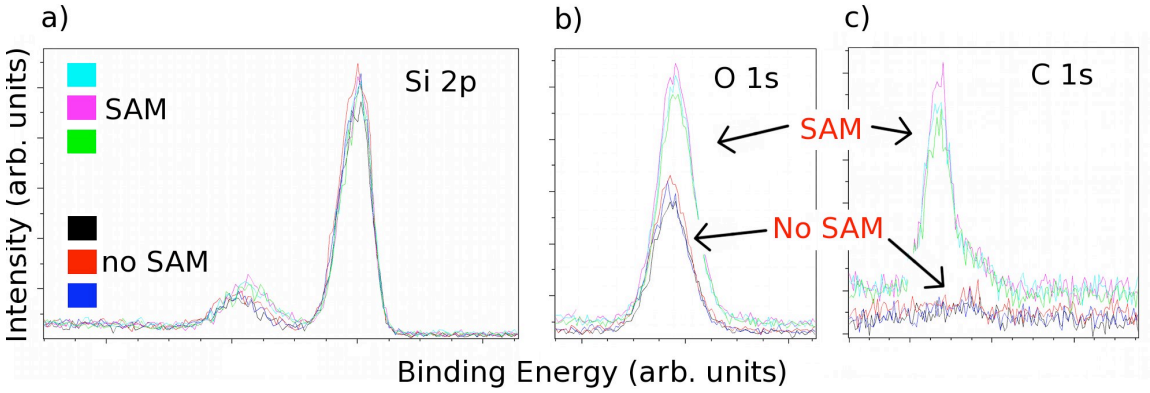

Figure 3.2. XPS for surface composition. Sample scans with 3 replications each for the SAM and no SAM samples (indicated by color legend), for Si 2p scans (a), O 1s scans (b), C 1s scans (c).

Angle resolved XPS was used to determine the thickness of the SAM using a standard overlayer model.[72,76] The angular dependence of the Si 2p peak intensity is given by:

$$I_{\mathrm{Si2p}} = I_0 \exp[-d/\lambda_{\mathrm{SAM}} \cos\theta],$$

where I_0 is the intensity in the absence of an overlayer, d is the thickness of the SAM, and λ_{SAM} is the photoelectron effective attenuation length (EAL) in the overlayer.[72,77]

The slope in the plot of the natural logarithm of the intensity as a function of $1/\cos\theta$ is equal to d/λ_{SAM} (Figure 3.3). In the model, the elemental Si 2p photoelectron signal seen at the detector is attenuated by the SAM overlayer. Due to the angular resolution of the analyzer, the data was fit up to 60°, to prevent passage of the signal originating from the sample holder. As noted by Fadley, an additional $\cos\theta$ dependence is expected at such grazing angles.

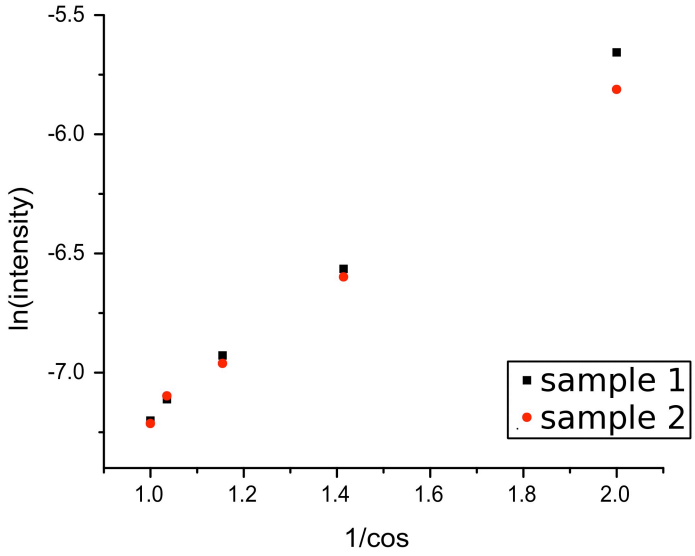

Figure 3.3. Plot of ARXPS data. The slope is determined from a linear regression fit. The slope is equal to d/λ_{SAM}.

The average value for the slope of the data in Figure 3.3 is 1.45 ± 0.08, where the error is reported as standard deviation across all samples. In order to extract the overlayer thickness, *d*, we need to calculate λ_{SAM} for the overlayer. The NIST Electron Effective Attenuation Length database program was used to calculate λ_{SAM}.[78] The EAL, λ_{SAM}, is a characteristic decay length of emitted photoelectrons and is dependent on material and

the value of the emission angle, θ. The parameters used for the calculation of λ_{SAM} using the NIST supplied software are included below. The values of λ_{SAM} are given at several emission angles and molecular weights to show that λ_{SAM} can be taken as constant for the purposes of ARXPS analysis (Table 3.1).

Table 3.1. Parameters for modeling EAL and calculated values of λ_{SAM}. The molecular weights given are the maximum and minimum for the polydisperse MPEOPS in bulk. The variation for different element composition of the polydisperse MPEOPS had negligible effect on the calculated value for λ_{SAM}. For the purposes of thickness calculation, λ_{SAM} was taken to be 3.53 nm.

Molecular Weight (g/mol)	θ (degrees)	λ_{SAM} (nm)
460	0	3.530
	30	3.522
	60	3.545
590	0	3.539
	30	3.531
	60	3.555

Because the overlayer model assumes that the substrate signal is semi-infinite, the native silicon oxide layer and the SAM both contribute to the attenuation of the signal:

$$d = d_{SAM} + d_{oxide}$$

We subtract the thickness of the native oxide (1.75 ± 0.05 nm, found from the ellipsometry measurements) to find the SAM thickness: d_{SAM} = 3.35 ± 0.27 nm. The

values measured for the thickness of the SAM by ellipsometry and ARXPS are in excellent agreement, indicating that this characterization is reliable.

3.3.3 Atomic Force Microscopy

Images of the AFM scans are shown in Figure 3.4. The bare silicon wafer is used as a control. The smooth features found from AFM together with the low incidence of MT adsorption indicate a continuous film of silane on the surface. An absence of defects, such as islands or pinholes, or contamination by unbound silane further establishes the antifouling nature. The root-mean-square roughness, R_{RMS}, was determined to be 0.51 ± 0.10 nm, consistent with a smooth, homogeneous silane layer.[37,79] As a comparison, the roughness of the bare silicon substrate measured under the same conditions was determined to be 0.14 ± 0.01 nm. For both the SAM and bare silicon wafer, the error is reported as the standard deviation across all samples measured.

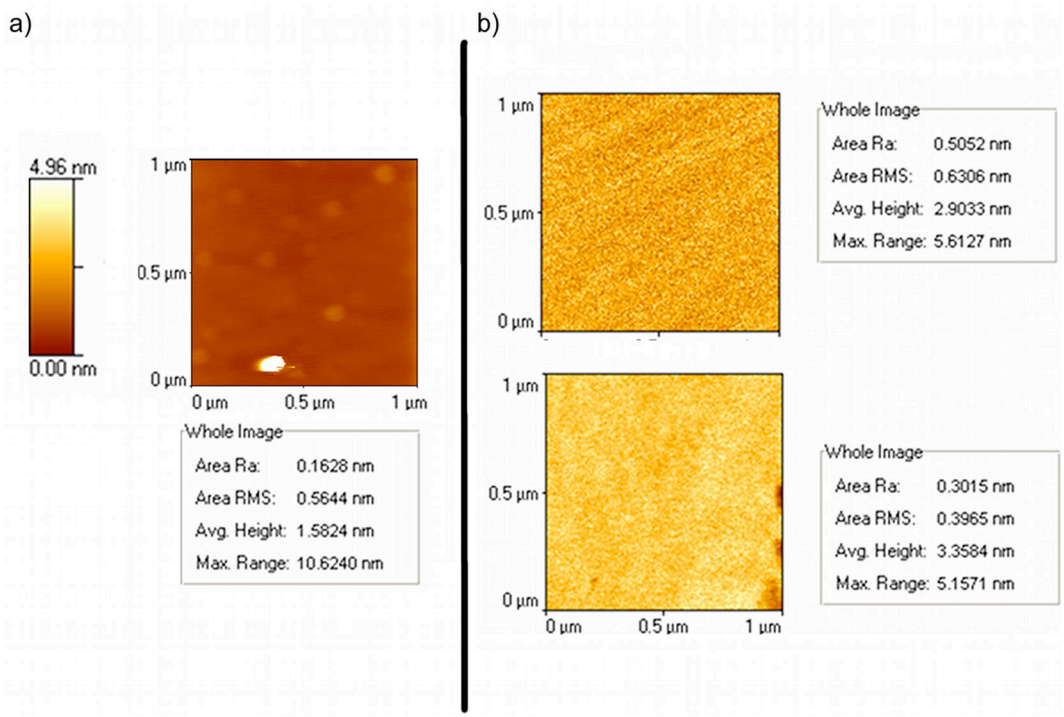

Figure 3.4. Sample AFM images of SAM and silicon oxide surfaces. Bare silicon (a) and PEG-SAM coated silicon (b) are shown. All images are scaled to 4.96 nm according to the color scale bar.

3.4 Discussion

3.4.1 SAM Formation

Here we propose a route for SAM formation in terms of the measured properties of the SAM and the experimental conditions used, all within the context of the extensive literature on SAM formation. The motivation for this is to understand how the structure of the SAM leads to its MT antifouling properties.

The thickness we measured for the SAM (3.35 nm) is close to that found for analogous PEG *thiol* molecules prepared under similar conditions, although it is somewhat higher than layers formed from MPEOPS using vapor deposition and a lower

concentration solution method.[46,61,70,75] The thicker layer presented here is likely due to the high solution concentration and long incubation time.[33]

We carry out a simple calculation using the SAM thickness and the molecular weight of the silane to estimate the surface density of silane molecules:

$$\sigma = \frac{N_A \rho d}{M_W},$$

where σ is the surface density in molecules per unit area, N_A is Avogadro's number, ρ is the volume density of bulk MPEOPS (1.08 g/cm^3), d is the measured film thickness, and M_W is the molecular weight of the PEG-silane (450-600). The range of molecular weights of the MPEOPS results in a range of surface density of the SAM from 3.53 to 4.71 molecules/nm^2. The lower density value is approximately 60% of the close packed maximum for PEG of 5.8 molecules/nm^2, indicating a densely packed monolayer.[46,80] The high surface density and the fact that the MPEOPS molecule has a length of 3.0-3.8 nm, approximately the thickness of the SAM, indicate a brush-like arrangement of the PEG chains.[70,81]

From our experiments, we can conclude that the SAM blocks MT adsorption well when formed from relatively high solution concentration of MPEOPS at an elevated temperature (75 °C) and a long incubation time. Combining this knowledge with the measured characteristics (thickness, surface density, and roughness) and reconciling this with a careful analysis of the literature on SAM formation allows us to propose a scheme for the formation and structure of the MPEOPS SAM developed in this study (Figure 3.5). Because no hydroxylation treatment was used prior to SAM formation, there was a

native initial concentration of silanol groups at surface of about 5 per nm^2, and a layer of adsorbed water (Figure 3.5a).[82] Also, because the MPEOPS solution was prepared fresh in toluene, which extracts water, there should be little polymerization of MPEOPS in bulk.[71,83] After immersion of the silicon wafer in the MPEOPS solution, silane molecules condense on the surface in a matter of minutes (Figure 3.5a).[84] Hydroxylation of one of the methoxy groups likely occurs, aided by the elevated temperature, requiring the presence of water, and releasing methanol vapor (Figure 3.5b).[62] As hydroxylation continues, silane crosslinking *between* erstwhile MPEOPS molecules and also *with* surface silanol groups occurs by siloxane bond formation (Si-O-Si), releasing water (Figure 3.5c). Finally, assembly completes with packing of the silane molecules (during which the PEG is oriented at the interface) and stabilization through further intermolecular and surface crosslinking, which is accelerated by heating (Figure 3.5d).[35,62,85] The omission of a catalyst or a priming surface hydroxylation suggests that the final number of surface anchored precursor molecules may be a fraction of the total monolayer, as low as 10-20% of the SAM, and still form a monolayer.[86] The remainder of the MPEOPS molecules likely form an extensive network of crosslinked siloxane bonds with dangling methoxy groups near the surface.[86,87] This crosslinking process is aided by the long incubation, baking and presence of ambient water in the oven after toluene evaporation.

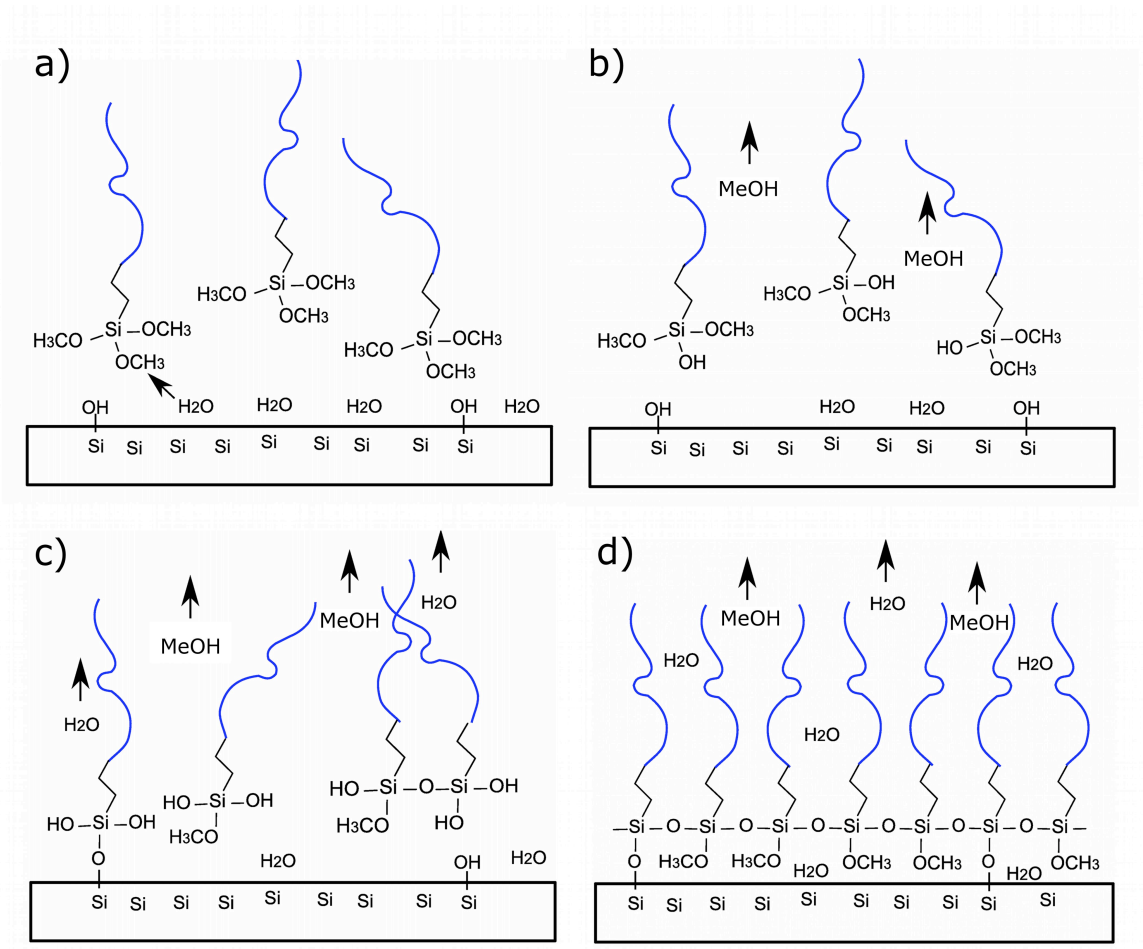

Figure 3.5. Proposed route of trimethoxysilane SAM formation. Methoxy terminated PEG chains are shown as blue curved lines. Methoxyl group reacts with water (a) to form hydroxyl group, releasing methanol (MeOH) (b). (c) Two hydroxyl groups react to form one siloxane bond, releasing water, in this way forming both silane-surface bonds and laterally crosslinked silane-silane bonds. After Krasnoslobodtsev, et al. and Finklea et al.[87,88]

SAM formation is very sensitive to environmental conditions, causing problems with reproducibility and disagreements in formation and structure in previous studies.[29] The reproducibility in the procedure we developed was observed for longer baking times, during which the toluene evaporates and the MPEOPS is forced to condense on the surface. Because the toluene was removed, more ambient water was able to access

the surface silanes increasing the likelihood of hydroxylation reactions, similar to what is described by Krasnoslobodtsev, et al.[88] Further, during initial stages the water content is controlled by the toluene, reducing the variation in this sensitive parameter.[89] In addition, because fewer steps are used in our procedure (no hydroxylation, no added hydrochloric acid or other catalyst), there is less chance for slight variations to alter the SAM formation.

Interestingly, the SAMs prepared here were thicker than previously studied SAMs made from the same molecule.[61,70] During SAM preparation, an increase in silane concentration has been seen to lead to an increase in grafting density, which likely explains the discrepancy as the higher surface density will lead to a greater extension of the polymer chain away from the substrate.[33,90] Also, the roughness values we obtained were consistent with previous AFM studies of MPEOPS SAMs and bare silicon wafers.[37,61]

3.4.2 Mechanism of MT-Resistant Behavior

Due to a lack of systematic study, the mechanism behind the protein-resistant properties of the PEG-silanes as a whole is not fully understood, although several interrelated factors have been shown to explain the observed phenomena. These factors which affect protein resistance include: steric repulsion by the flexible PEG chain, the distal chemistry and surface density of the grafted molecule, the hydration of the SAM, and the size and surface properties of the proteins.[26,42,80,91] Early models for the protein antifouling of polymer surfaces focused on steric repulsion; where compression of the

elastic polymer establishes a restoring force that opposes the protein's attraction to the surface (Figure 3.6).[92] Under this model, densely packed, long chain polymers should provide the best protein-resistant surface. However, several experiments showed that some densely packed (and more ordered) SAMs did not resist protein adsorption as well as amorphous SAMs that were otherwise identical because the dense packing concentrates the distal endgroups, which interacted with the protein.[46,50] Thus, for densely packed monolayers to prevent protein adsorption, it is essential that the distal tail group (a methoxy group in this work) does not bind with the protein. Because, in our study, distal methoxy groups are present at the solution interface, it is evident that these groups do not promote MT binding.

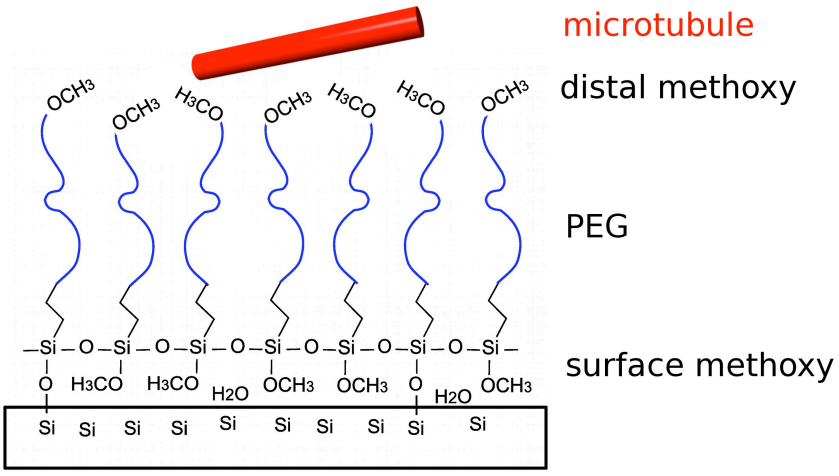

Figure 3.6. Molecular basis for protein antifouling. Distal methoxy groups do not bind MTs. PEG sterically blocks MTs from reaching surface. Surface methoxy groups act as final barrier to MT adsorption. Not to scale.

Following the analysis of the formation mechanism, we infer that a single siloxane bond formed from one of the methoxy head groups while the other two methoxy groups either

remain intact or crosslink to neighboring silanes (Figure 3.5d).[62,87] This would present two fronts for preventing MT adsorption: a disordered layer of methoxy and crosslinked silanes near the silicon surface in addition to the distal methoxy group. As noted by Satulovsky, et al., these 'layers' will provide good kinetic and equilibrium passivation: the methoxy-capped PEG brush presents a steric barrier to approaching MTs (kinetic) while the methoxy groups and lateral siloxane crosslinkers near the surface reduce the number of binding sites for the MTs (equilibrium).[91] Correspondingly, it is possible that the SAM formed at lower concentration and baking time did not reliably prevent MT adsorption because the lower silane surface density allowed the PEG chains to lie down on the surface, reducing the steric repulsion of MTs.

3.5 Conclusion

From our characterization of the MT resistant SAM introduced in Chapter II, we concluded that the MPEOPS formed a smooth and continuous film of monolayer thickness with a high surface density of silanes (3.5 - 4.7 molecules/nm^2). Through comparison with previous studies, we were able to postulate the route for formation of the SAM. The SAM formation likely occurs through replacement of a single methoxy group with a siloxane bond to the surface silicon with two methoxy groups able to remain intact or crosslink to neighboring silanes. It was further evident from the high density, that the PEG chains were extended out from the surface with the distal methoxy group and that this group did not interact with MTs.

The protocol we developed for SAM formation is a new facile method, being one step, which uses a commercially available silane and no costly investment in time or equipment. If this method proves successful at preventing fouling of other proteins and macromolecules, it may find widespread use in research that interfaces biological and synthetic materials.

CHAPTER IV

PATTERNING AND MANIPULATING MICROTUBULES

4.1 Introduction

Once surface fouling of MTs has been prevented, immobilization may be attempted. In the past, surface immobilization of proteins, DNA, cells and microspheres has been achieved through nonspecific adsorption, ligand-receptor binding and chemical crosslinking.[93-97] Several studies have employed these methods for immobilizing MTs.[41,98,99] While these methods are suitable for assaying phenomena such as adsorption kinetics, they do not allow for on-demand, reversible adsorption and orientation because the surface begins binding the target molecules immediately after their introduction. Additionally, several works have made use of the highly specific interaction between MTs and kinesin (a motor protein) to immobilize and orient MTs in microfluidic channels.[19,100-104] In these studies, surface bound kinesins were used to capture and bind MTs while casein was used to passivate the surface against MT adsorption. Because kinesin binds MTs at-will and because the duration of the attachment is determined by the kinesin-MT binding kinetics, these methods are of limited use in MT patterning and manipulation. In order to provide the active manipulation and on-demand adsorption desired, we employ external forces through DC electrophoresis. Electrohydrodynamic forces supplied by electrophoresis and magnetic fields are compatible with MTs, programmable and are readily incorporated into electrochemical sensor assemblies.[60,105-109]

4.2 Integrating SAMs and Lithographic Patterns

4.2.1 Background

In the past, SAM patterning has been achieved through various means with the most successful methods being microcontact printing (MCP), dip-pen nanolithography (DPN), electron beam lithography, and UV lithography.[38,110,111] When deciding on the best method for patterning, one must coordinate the actual pattern transfer technique (i.e. lithography, microcontact printing, etc.) with the materials to be patterned in order to design a workable scheme. For example, standard positive tone lithography is widely used for patterning SAMs by exposure and development of poly(methylmethacrylate) (PMMA) resist or a similar mask layer, followed by deposition of a SAM to the cleared substrate (Figure 4.1a).[97,112-118] However, solution deposition of the SAM (as used in this dissertation) at this stage is not acceptable because the SAM solvent will most likely dissolve or deform the PMMA mask. This can be avoided by using vapor deposition of the SAM or water-soluble SAM precursors, as PMMA is not easily dissolved in water.[114,118] Also, backfilling by a second SAM allows crossmixing of the SAM molecules, which are surface mobile.[114]

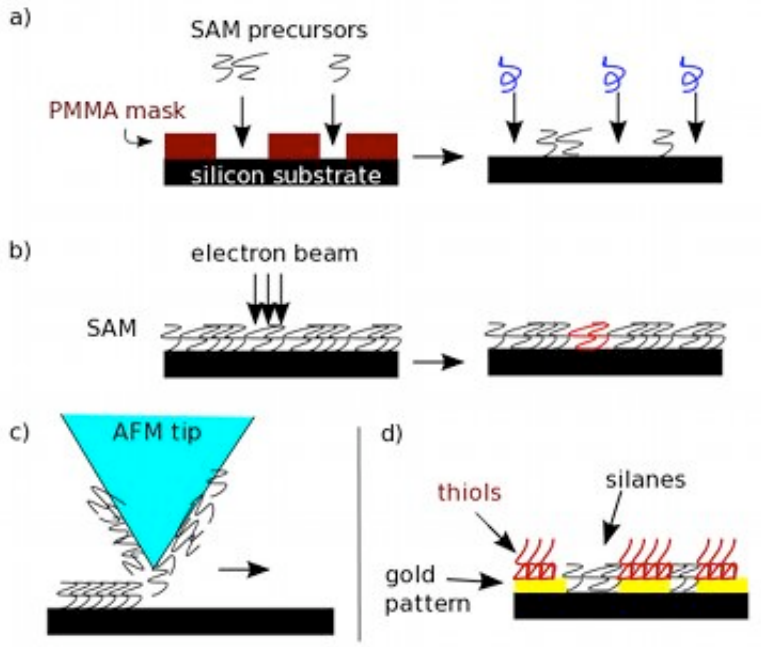

Figure 4.1. Schemes for patterning with SAMs. (a) Positive EBL with developed PMMA for masking 1st SAM deposition. After liftoff, the remaining area may be backfilled by a second SAM. (b) Selectively altering existing SAM chemistry by exposure to electron beam. (c) Direct deposition of SAM molecules by DPN. (d) Chemically selective surface deposition with thiols depositing on Au and silanes on silicon.

Alternately, the SAM itself may be used as a mask layer that may be chemically altered or physically removed by exposure to an electron beam, UV or AFM tip (Figure 4.1b).[41,119-123] This method is limited in choice of materials which chemically react upon beam exposure and it is also difficult to fully remove the crosslinked material.[38] A third method that avoids problems with SAM crossmixing and solvent incompatibility is direct printing of the SAM molecules by DPN or MCP (Figure 4.1c).[34,111,124-127] However, MCP with silanes has not been well-developed and it is not possible to pattern true nanoscale features with MCP, while DPN is technically challenging and slow, allowing water to react with the silanes before printing.[114] In a fourth method, the strong

affinity of SAM precursor molecules for specific surfaces, i.e. silanes for SiO_2 and thiols for Au, allows for chemically selective adsorption to predetermined patterns (Figure 4.1d).[128-131] Again, crossmixing and desorption of the binary SAMs presents problems, and this method also requires the use of the less stable thiol based SAMs.[35,114]

For this work, we have chosen two methods for patterning with the MT resistant PEG SAM presented in the previous chapters. The first is a modification of the standard EBL method shown in Figure 4.1a above. In this scheme, the SAM is formed prior to lithography and an Au layer is patterned on the SAM by EBL, referred to as an 'unpassivated pattern' (Figure 4.2a). The Au can be then be used as an electrode for attracting MTs or further chemically functionalized. For the second method, an Au pattern is first fabricated and then the PEG SAM is formed over the entire surface, this is referred to as a 'passivated pattern' (Figure 4.2b).

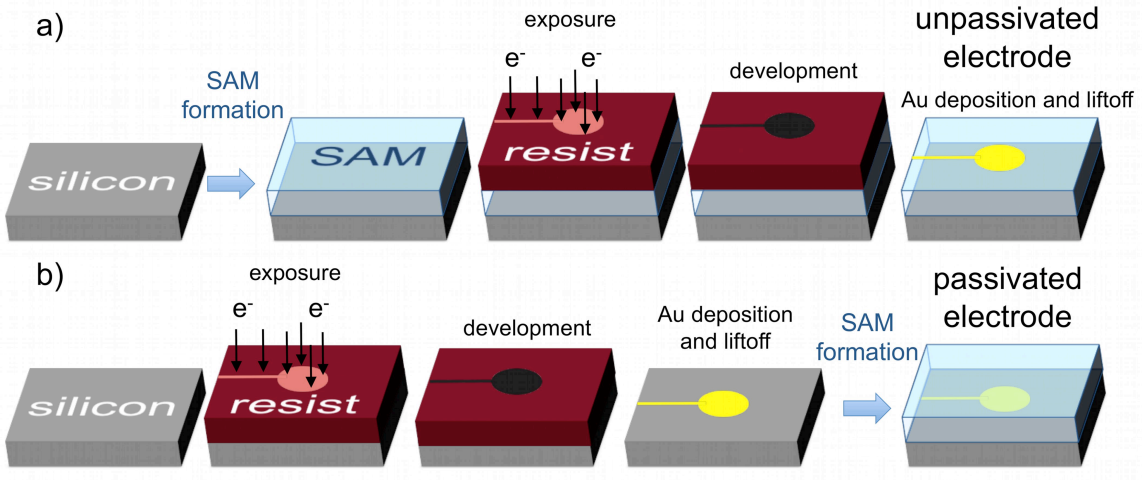

Figure 4.2. Patterning MT-resistant PEG SAMs with EBL. The steps are shown for fabricating the unpassivated pattern (a) and passivated pattern (b).

There are significant benefits to integrating the SAM with lithographic patterns in this way. First, by forming the SAM in a separate step, we avoid unwanted interaction of the SAM molecules with the solvent-sensitive EBLresist layer. Further, this does not require patterning of the SAM molecules themselves; a difficult task, as shown by the existence of only a few successful, high-cost methods. We are only required to pattern the Au layer, a process which is well developed for fabricating structures down to ~ 10 nm, the scale of single proteins. EBL also allows us to design a wide variety of pattern geometries without the need to make masks (photolithography) or masters for printing (MCP). The EBL system was located in-house in the Center for Nanoscale Science and Technology in the Texas A&M University Department of Physics.

4.2.2 Materials and Methods

4.2.2.1 Electron Beam Lithography

All patterns were fabricated using positive tone electron beam lithography. Silicon wafers with native oxide were cut to approximately 1x1 cm and cleaned using the standard acetone/ isopropanol procedure outlined above. Electron-beam resist (PMMA, 3% w/v in chlorobenzene) was spun onto the wafers (4000 rpm for 40 sec) then cured on a hot plate at 160 ºC for 90 seconds. A JEOL 6460 electron microscope equipped with NanoPattern Generating Software controllers (JC Nabity) was used for e-beam writing. After exposure, patterns were developed with MIBK in isopropanol (1:3) for 70 seconds followed by thermal vapor deposition of a 3 nm chromium adhesion layer and 12 nm of

gold. The substrates were then placed in acetone for 30 minutes to lift off the remaining PMMA.

4.2.2.2 SAM Preparation and Passivation Assays

The SAM preparation procedure described in Chapter II was used for both passivated and unpassivated patterns. The unpassivated pattern was fabricated by first forming the SAM on the silicon substrates, spinning on PMMA resist, then continuing with standard positive tone electron beam lithography (Figure 4.2a). The passivated pattern was fabricated by first making a gold pattern on the silicon substrate, then overlaying with a SAM (Figure 4.2b). Passivation assays were carried out as described in Chapter II.

4.2.3 Results and Discussion

Passivation assays were carried out to ascertain the ability of the PEG SAM to retain its MT-resistant nature after patterning. For the unpassivated pattern, the results show that the SAM retains its nonfouling qualities while the unpassivated gold promotes nonspecific MT adsorption (Figure 4.3). This method presents a surface with binary properties: regions with high affinity for MTs (gold) adjacent to regions of low affinity (SAM). Because the gold remains exposed, a wide variety of additional modification can be achieved by using the gold pattern as a template for thiol functionalization.[132]

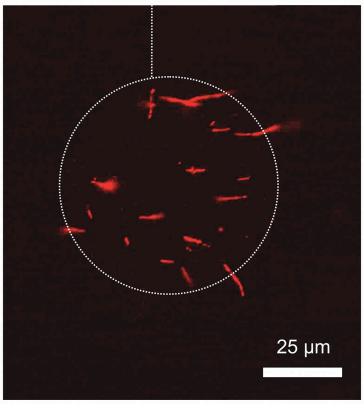

Figure 4.3. Nonspecific adsorption of MTs on Au. The Au disc is not passivated, allowing MTs to nonspecifically adsorb immediately upon their introduction. The surrounding SAM remains free of MTs, showing that the antifouling nature is retained through the lithographic processing.

For the passivated patterns, no MT adsorption was seen on 60 µm diameter disc patterns, even though we did observe MT adsorption on larger patterns (> 100 µm). Although, silane SAMs are most often formed on silicon oxide, they are known to crosslink laterally, as discussed above, which may explain the ability of the SAM to passivate the smaller gold patterns.[31,87,133] As discussed in Chapter 3, it is likely that the SAM is able to bridge smaller features by lateral crosslinking, but over large distances the lack of surface grafted siloxane anchors prevents stable and complete SAM formation.

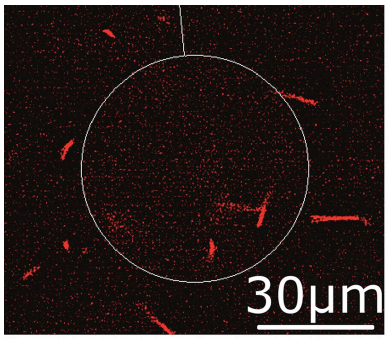

Figure 4.4. Passivated pattern. No MT fouling is seen on passivated patterns below about 100 μm in diameter. The MTs seen are freely diffusing near the surface, not bound as those in Figure 4.3.

Due to the robust nature of the SAM, the integration of SAM and Au lithography is straightforward, requiring no modification to either the standard positive tone EBL procedure or our SAM protocol. This method is versatile in that photolithography may be used in place of EBL. Further, this method is quite general and may be used for patterning other biomolecules so long as they do not foul on the MT resistant SAM.

4.3 Patterning and Manipulating MTs

4.3.1 Background

As mentioned above, electrophoresis is compatible with the sensitive nature of MT solutions and has been used to control the motion of MTs and other biomolecules.[134,135] However, electrophoresis of MTs has so far been relegated to analyzing fundamental properties such as dielectric constant, dipole moment, MT charge, and mechanical stiffness, and successful application of electrophoresis for MT patterning and manipulation, much less the assembly of multiples MTs, has not been

demonstrated.[107,136,137] Here we present passivated and unpassivated electrodes for controlling MT patterning and alignment using electrophoresis. We show that, remarkably, the PEG SAM is able to passivate the Au electrodes, an effect likely due to the high density of SAM molecules mentioned in the previous chapter. Because of this, for the first time, we are able to demonstrate reversible on-demand adsorption and patterning of MTs. We further show patterning and alignment of single MTs on 1 μm wide gold lines. Tracks of nonpolarly aligned MTs, which are tens of microns in length and less than 100nm wide (approximately 1-3 MTs wide), are also presented. Some minor results on controlling MT polarity and alternate electrode pattern geometries are included in section 4.3.3.3 and 4.3.3.4, respectively.

4.3.2 Materials and Methods - Flow Cell for MT Electrophoresis

In order to control MT patterning and orientation to a higher degree than that obtained from the passive adsorption on gold (Figure 4.3), we applied a DC potential across the flow cell to induce electrophoretic migration of the MTs. Because the isoelectric point of tubulin is approximately 5.4, the MTs are negatively charged when suspended in buffer at pH 6.8. Upon application of a potential, the MTs migrate to the lithographically patterned gold, which acts as the anode. A glass coverslip coated with Cr and Au (2 nm and 4 nm, respectively) was used as the counter electrode (Figure 4.5).

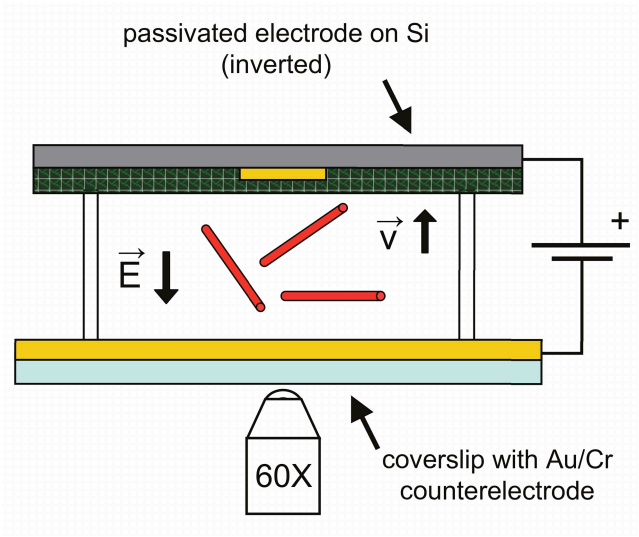

Figure 4.5. Flow cell assembly for electrophoresis. Flow cell (Figure 2.1) modified to include electrodes.

The thin counter electrode transmits light, allowing the patterned surface to be imaged through it. Using a DC power supply, potentials up to 1.5 V were applied vertically through the flow cells with approximately 60 microns between the electrodes. Above about 1.2 V, the likelihood for formation of gas bubbles (due to electrolysis) and MT depolymerization increased dramatically. It should also be noted that application of a constant DC current rather (than a potential) as low as 10 μ A quickly induced electrolysis due to the current source attempting to force the current through the increasingly resistive flow cell, discussed in greater detail in Chapter V. When desirable, unbound MTs were flushed away as in the passivation experiments. To prevent lateral fluid flow in reversible binding experiments, we found it necessary to prevent evaporation from the open ends of the flow cell by sealing them with nail polish.

4.3.3 Results and Discussion

4.3.3.1 On-demand Reversible Adsorption

On demand, reversible MT adsorption is shown in Figure 4.6 and Supplementary Video 1 for a 60 μm passivated disc electrode. Upon introduction of MTs, prior to application of the potential, there is no adsorption of MTs on either the electrode or substrate due to the passivating monolayer (Figure 4.6a). Remarkably, even those MTs that are very close to the electrode are seen to be unattached, indicating that SAM layer effectively passivates the electrode. (see supplementary video).

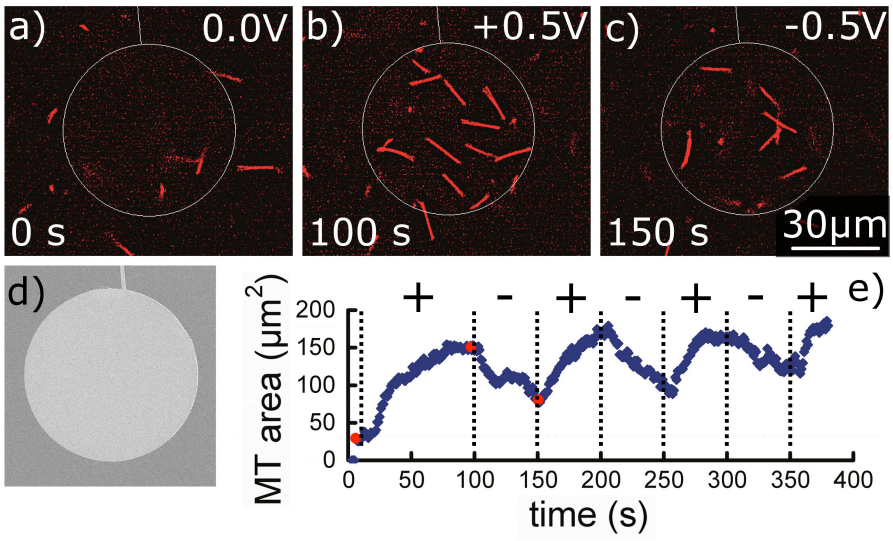

Figure 4.6. Reversible MT adsorption on passivated disc electrodes. (a) Initially, the electrodes are grounded and there is no adsorption. (b) MTs are concentrated on the disc for 100 s at +0.5 V DC. (c) The potential is then reversed to drive MTs away for 50 s. White lines indicate edges of electrode (a-c). (d) Scanning electron microscopy (SEM) image of a disc electrode. (e) Plot of area covered by MTs on the electrode as a function of time with +0.5 V and -0.5 V applied alternately; images (a-c) are taken from the same experiment and are indicated in the plot with a red dot. See Supplementary Video 1.

When the potential is switched on, MTs migrate to the anode, localizing at the pattern while the surrounding regions remain free of MTs (Figure 4.6b). The MTs that are in focus are located very near the plane of the disc electrode. Upon reversal of the potential, the MTs are driven away from the pattern (Figure 4.6c). Despite application of the positive and negative potentials for equal time, a gradual increase in the number of MTs can be seen near the electrode even though the surface continues to remain free of fouled MTs. This may be due to a higher drag coefficient acting on MTs moving away from the surface which is caused by the presence of the surface itself.[138] A discussion of this affect is presented in Chapter V. The process of adsorption and repulsion can be repeated until the MTs begin depolymerizing from fluorescence exposure (approximately 30 min.), making it possible to switch the pattern between 'MT on' and 'MT off' states (Supplementary Video 1). This type of reversible adsorption may lead to ordered, multiple MT structures and aid in the polar orientation of MTs. This is based on the phenomena of reversible interactions causing crystal formation, and has been discussed by Whitesides, et al.[139]

4.3.3.2 MT Patterning and Alignment

This method of reversible, at-will MT adsorption may prove useful for guiding MTs to assemble into more organized filamentous structures. Toward this end we tested the ability of the current system to capture and align microtubules on narrow gold electrodes. We found that high aspect ratio passivated electrodes are able to orient MTs to the shape of the pattern after the filaments reach the surface (Figure 4.7,

Supplementary Video 2). Lines and rings were fabricated with line widths of 1 μm and a potential was applied as above. As with the disc electrode, there was no MT adsorption prior to application of the potential (Figure 4.7b). Upon application of 1V, MTs rapidly adsorb at high density to the ring (Figures 4.7c-e, Supplementary Video 2). In order to allow MTs to adsorb at high density, a relatively high final concentration of MTs was used (25 nM). A careful inspection of the images indicates that MTs preferentially align in a parallel direction to the line at the top of the ring and tangent to the ring itself. Because the MTs begin to overlap very quickly, it is difficult to determine the extent of this alignment.

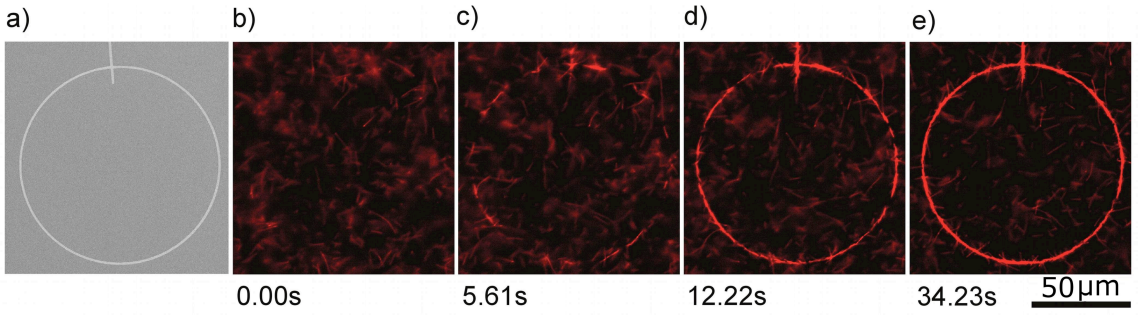

Figure 4.7. MT adsorption and alignment on ring electrode. (a) SEM image of ring electrode. The Au ring has a line width of 1 μm and a diameter of 100 μm. (b-e) Time course of MT adsorption after +1.00 V is applied to the electrode at 0.00 s. See Supplementary Video 2.

To observe the adsorption process more closely, the concentration of MTs was reduced by one half to 12.5 nM, and the experiment was repeated. Figure 4.8 is a series of images that show the adsorption and alignment of a single MT to the same size ring electrode as in Figure 4.7 at higher magnification. The images are all focused in the plane of the gold pattern. The microtubule is out of focus at 2.68 s and comes into focus as it adsorbs to

the ring at 4.20s. We note that the area surrounding the electrode remains free of MT fouling. See also Supplementary Video 3.

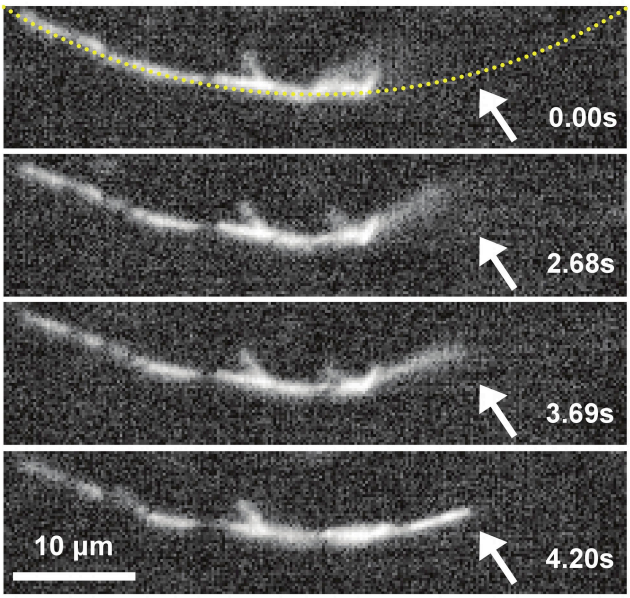

Figure 4.8. Individual microtubule aligning on ring electrode with +1.2 V applied. Dotted line indicates the path of the underlying gold electrode. Time elapsed from the first frame is indicated in seconds. White arrow indicates a single MT adsorbing to the ring.

These results indicate that MTs are able to quickly align on the electrode surface once the potential is applied. We postulate that the low interaction of the MT with the SAM layer on the passivated electrode promotes this high degree of orientation (as compared to the unpassivated gold) as it allows the MT to reposition after making initial contact with the surface. It should be noted that the smaller the gold pattern, the higher the potential required for inducing electrophoretic motion of the MTs. As a result, many of the MTs adsorbed to the ring electrodes in Figures 4.7 and 4.8, remain after the potential is removed. This higher potential exerts a stronger force on the MTs initially and may be strong enough to overcome the steric repulsion of the SAM.[91] It is also

possible that the high field near the electrode attracts the flexible PEG chains of the SAM to the surface, deactivating its passivating properties.[91] Additionally, it is evident from our observations that interactions between MTs may prevent some filaments from completely aligning on the electrode, as seen at the bottom of the arc in Figure 4.8.

4.3.3.3 Modifications for Controlling Polarity

Ultimately, because MT-motor interactions are based around the polar orientation of microtubules within the cell, one must control MT polarity to create truly functional tracks for motor based transport and sorting devices.[1] In a few cases, polar MT orientation in a cell-free environment has been achieved using MT nucleators such as centrosomes, kinetochores, and γ-tubulin, and surface bound kinesin (dynein) motors, which orient MTs by propelling their minus (plus) end forward (Figure 4.9).[13,100,101,140-146] Polar growth of MTs using synthetic microtubule organizing centers has recently been developed by anchoring the minus ends of short MTs onto microbeads and extending the MTs radially outwards by plus end specific polymerization using NEM.[147] Polar orientation of MTs by anchoring one end of the MT to glass or silicon and using fluid flow to force the other end to orient in the downstream direction was also shown.[148,149]

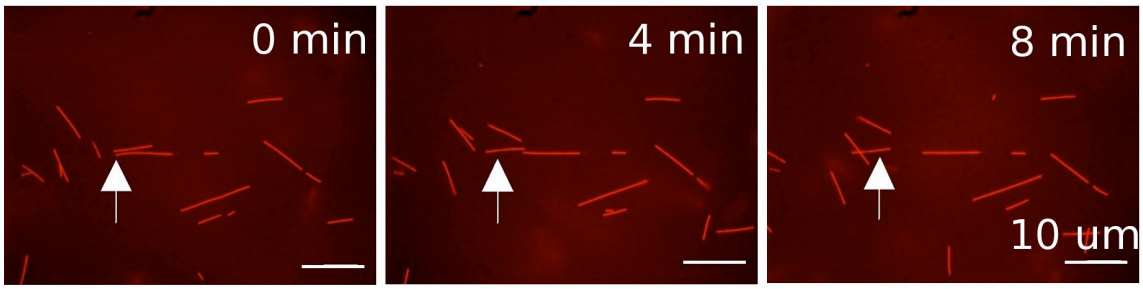

Figure 4.9. MT motility assay. White arrow is stationary relative to flow chamber. Surface immobilized kinesins push MTs along rather than kinesin traversing on immobilized MTs (see Figure 1.1b).

It should be noted that nonpolar collinear orientation of MTs has been achieved by dielectrophoresis, which acts on the asymmetric polarizability of the MT to orient it in an AC electric field, and also by external magnetic fields acting on both magnetically labeled and normal MTs.[107,150] Although all of these methods succeeded at polarizing MT orientation, none directly controlled the organization of multiple MTs or localized MTs to patterns.

As an application of the reversible adsorption method described above, we attempted to observe the polarity of MTs localized on the passivated electrode. Polarity marking of MTs was done by incorporating the minus end polymerization inhibitor, N-ethylmaleimide (NEM), and highly rhodamine labeled tubulin into the tubulin polymerization protocol.[151] This resulted in MTs that were bright at the minus end and dimmer at the plus end (Figure 4.10). As a further extension, biotin labeled tubulin was incorporated at the minus end so that fluorescent streptavidin proteins could be specifically bound to this part of the MT. Details of the protocol are included in

Appendix B. Once MTs were polar labeled, they were introduced and the procedure for reversible adsorption outlined in section 4.3.3.1 was followed.

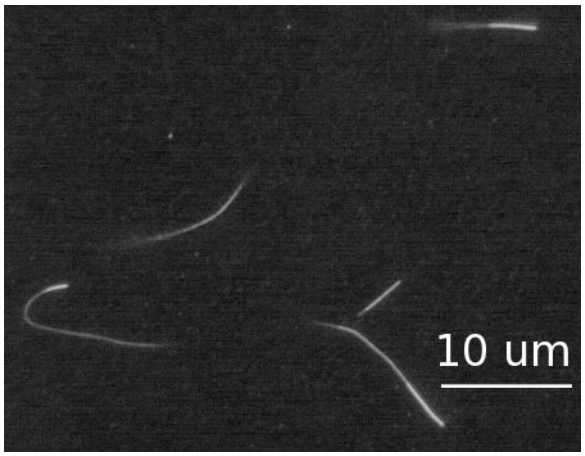

Figure 4.10. Polarity marked MTs. Minus end has higher ratio of rhodamine labeled to unlabeled tubulin and is therefore brighter.

The results for this experiment were unclear. Polarity marked MTs could be seen to move towards the electrode, but a preferential polar orientation was not seen. This is most likely due to the nature of the electrophoretic force and the molecular structure of the MT that determines its polarity does not interact with the electric field in an asymmetric manner. It is possible that an asymmetry could be produced at one end of the MT by (1) reducing the surface charge by cleaving off the C-terminus of the tubulin dimmer or (2) increasing the surface charge or viscous drag by labeling the end with additional molecules.

4.3.3.4 'Antennae' For Increasing E-Field Density

A less successful, but nevertheless interesting experiment carried out was to determine whether we could increase the number of MTs on the pattern by increasing the cross

sectional area of the electric field region without using large continuous regions of Au. This would prevent problems arising from incomplete SAM passivation on larger structures, mentioned in section 4.2.3. Further, it allows us to view alignment of single MTs on linear electrodes rather than the circular type in section 4.3. Although this 'antennae' pattern should decrease the current density for a given potential, it should also increase the number of MTs in the central, higher density field region, which in turn would increase the number of MTs that migrate to the pattern.

We made antennae patterns by fabricating 200 nm Au lines (or circles) that connected larger 1 micron lines (or circles). We then used the same method for patterning the MTs on the rings described above (Figure 4.11).

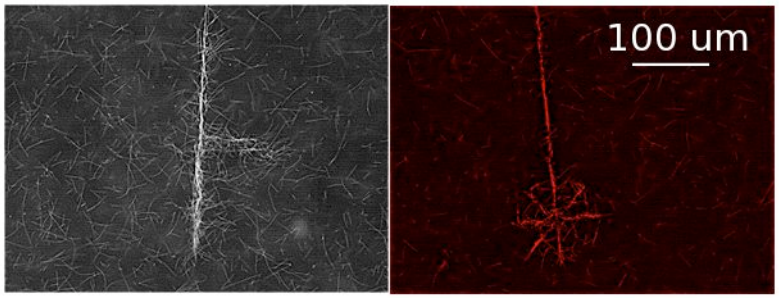

Figure 4.11. Antennae pattern for increased field density. 1 μm lines are connected with and surrounded by smaller 200 nm lines.

The results show that the MTs were increased in density on small features as compared to the single 1 μm line. It appears however that MT-MT interaction prevented a high degree of alignment to the pattern. The best method we have found thus far for preventing this inter-MT is to reduce the concentration of MTs; however this creates a problem when attempting to form continuous tracks if the few MTs that are present do not cover the entire pattern, as fresh MTs can not be introduced once the flow chamber

has been sealed. Thus, the solution would seemingly lie in finding an alternate method for preventing fluid flow, which does not permanently seal the chamber. We did make several unsuccessful attempts to achieve this, which included using temporary sealants like silicon grease and tape, and creating a large reservoir of buffer around the openings of the flow chamber.

4.4 Conclusion

The results presented here show that the PEG-silane SAMs prevented MT adsorption effectively and could be integrated into electron beam lithography in a straightforward manner. The SAM was integrated with lithographic patterns as either a nonfouling sublayer or overlayer, and then patterning and orienting MTs using DC electrophoresis demonstrated the utility of this method. Because the electrophoretic assembly of MTs on the SAM overlayer is easily reversible, the technique has a distinct advantage over methods which employ chemical binding or protein-ligand crosslinkers (such as biotin and streptavidin) and does not require fabrication of microfluidic channels to confine the MTs. Further, by patterning MTs using the nonfouling SAMs as opposed to patterning the SAMs themselves, we avoided the complications which arise in many of the previous SAM patterning techniques discussed in Section 4.2.1.

CHAPTER V

MECHANISM AND NATURE OF MT MIGRATION

5.1 Introduction

In this section, we analyze the MT migration behavior of the MTs under the conditions used in the patterning experiments. The discussion includes the forces acting on the MT, the time dependence of the MT migration and the dynamics of the ions in the flow chamber. The aim is to understand the fundamental forces behind the observed phenomena as well as to improve upon the experimental design for achieving higher control over MT manipulation. We show the buffer ions cannot reach an equilibrium state during the time scale of the experiment as the E-field in the chamber would completely screen the field within 20 nm from the surface and MT migration would not be possible. Thus, we discuss how non-equilibrium phenomena such as buffer ion dissociation and migration more accurately describe the system.

We posit that the progression of events during MT patterning is as follows: 1) apply potential, 2) high mobility ions migrate, creating a transient electrical current that decays in milliseconds, 3) surplus buffer salts in the center of the chamber dissociate (time scale?), 4) MT migration decays (~ minutes). The significance of these events and the methods for arriving at the time scales are discussed below. The discussions in this chapter will assume that electrolysis is not occurring (during experiments, electrolysis would occur at potentials above about 1.5 V as seen by the formation of gas bubbles at the electrodes).

By measuring the area of the electrode covered by MTs as a function of time (section 4.3.3.1), we can see a general trend of steadily increasing MT coverage that eventually decays towards a constant value, indicating that MTs are no longer reaching the electrode (Figure 5.1). The question then becomes: what is behind these phenomena? In our experiment, an applied potential imposes an electric field in the electrolyte containing buffer solution located between the two electrodes, which, in turn, induces an ionic current, so that the flow chamber is essentially a simple electrolytic capacitor.

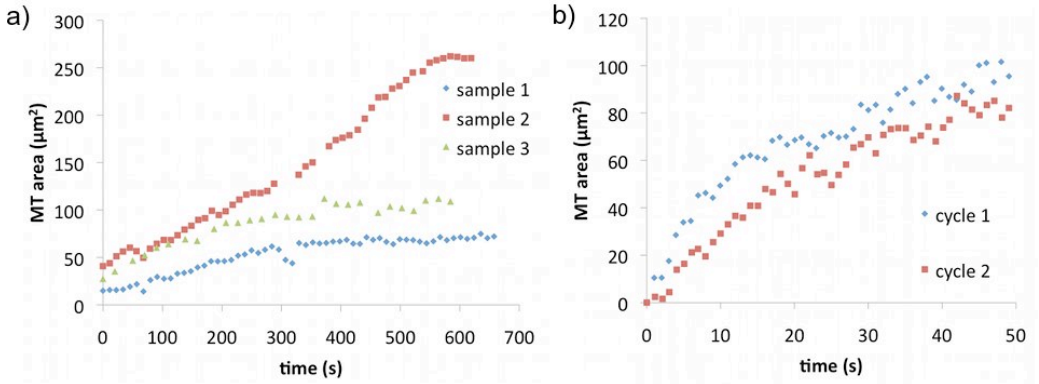

Figure 5.1. Decay in MT migration as a function of time. a) sample curves for decay at high MT concentration at 1.0 V. b) First two cycles from Figure 4.6. At low surface density the area of the electrode covered by MTs is proportional to the number of MTs (Appendix A).

Another phenomenon we observed was a threshold potential below which there was no MT migration over the lifetime of the MTs (about 1 hour in this setup). To understand this behavior, we consider two possible causes 1) the minimum force required to achieve deterministic motion in the face of randomizing thermal forces, and 2) a natural electrode polarization due to buffer ion accumulation. We then compare this with the calculated force applied using our experimental configuration.

5.2 Electrophoresis of MTs

Most studies on electrophoretic migration of microtubules use large capillary-style flow chambers capable of maintaining a constant current, which, from Ohm's law, is the result of a constant E-field:

$$\vec{E} = \rho\vec{j}, \tag{5.1}$$

given that ρ, the resistivity of the buffer solution, is a constant parameter, and $\vec{j}$ is the current density.[135] In this case, the migration velocity of the MTs is constant in time, and from Equation 5.1, we see that:

$$v = \mu E = \mu\rho j. \tag{5.2}$$

where μ is the electrophoretic mobility. The electrophoretic mobility is a proportionality constant between the migration velocity and the electric field, and is based on the principle that small particles migrate at their terminal velocity, and that this velocity is linearly dependent on the electric field strength.[135,152] We note that, because the geometry of our flow chamber does not incorporate charged sidewalls, we do not see bulk fluid flow from electroosmosis, which can dominate the MT migration behavior in microfluidic channels.[135] The absence of bulk flow from electroosmosis and convection was determined by replacing the MTs with uncharged microbeads (Appendix C).

5.2.1 Poisson-Boltzmann Solution for Electric Field

Because, the MT migration occurs after the initial decay in charge current, it is reasonable to assume that the ions have reached equilibrium without completely

screening the electric field, and that there is some residual field, E_{eff}, remaining which induces migration according to Equation 5.2: $v = \mu E_{eff}$. However, we show here, through a straightforward evaluation of the Poisson-Boltzmann equation for the electric field near the electrode, that the field would be completely screened out by counterions within 20 nm of the electrode surface. In the following section, we explain the phenomena using a non-equilibrium description where E-field is present in the central region of the flow chamber, and low currents are flowing due to continuous dissociation of neutral buffer molecules.

Several assumptions will be made for the following discussion. First, we will consider the flow chamber as one-dimensional with two infinite conducting parallel plates, and a buffer solution in between. The size of the lithographic pattern is quite small, so this will be an approximation that does not include the asymmetry of the electric field. Second, we assume that no interactions occur at the gold surfaces, or 'blocking electrodes'. As gold is a relatively inert material, and we purposely avoid electrolysis in the flow chamber, this assumption is quite reasonable. Third, to simplify the description, we ignore the contribution of MTs to the electric properties of the chamber, and assume that the PIPES molecule is the dominant electrolyte in the flow cell.

Using Poisson's equation, the charge distribution near an electrode is readily calculated at equilibrium (Appendix D). At equilibrium, the particles follow Boltzmann statistics, $n_i(\Phi) = n_i^0 z_i e^{-\beta e z_i \Phi}$, for which an analytical solution can be obtained in the one-dimensional case, where Φ is the potential, n_i and n_i^0 are the number concentration for

species i, with and without potential, respectively, z is the charge number, e is the elementary charge, and β is the reciprocal of the product of the temperature and Boltzmann constant.[153] One way to conceptualize the system is through considering the characteristic distance over which the E-field is screened, the Debye length, which is derived from the Poisson-Boltzmann equation:

$$\lambda_D = \sqrt{\frac{\varepsilon_0 \varepsilon_r k_B T}{2 N_A e^2 I}}, \tag{5.3}$$

where ε_0 is the permittivity of free space, ε_r is the relative permittivity, T is the temperature, N_A is Avogadro's number, and I is the ionic strength.

In Appendix D, we calculate the E-field as a function of distance from the electrode, assuming the presence of dissociated PIPES and $MgCl_2$, shown in Figure 5.2 for 1 V and 0.1 V potential. The details of the calculation and the concentrations of the components are given in the Appendix.

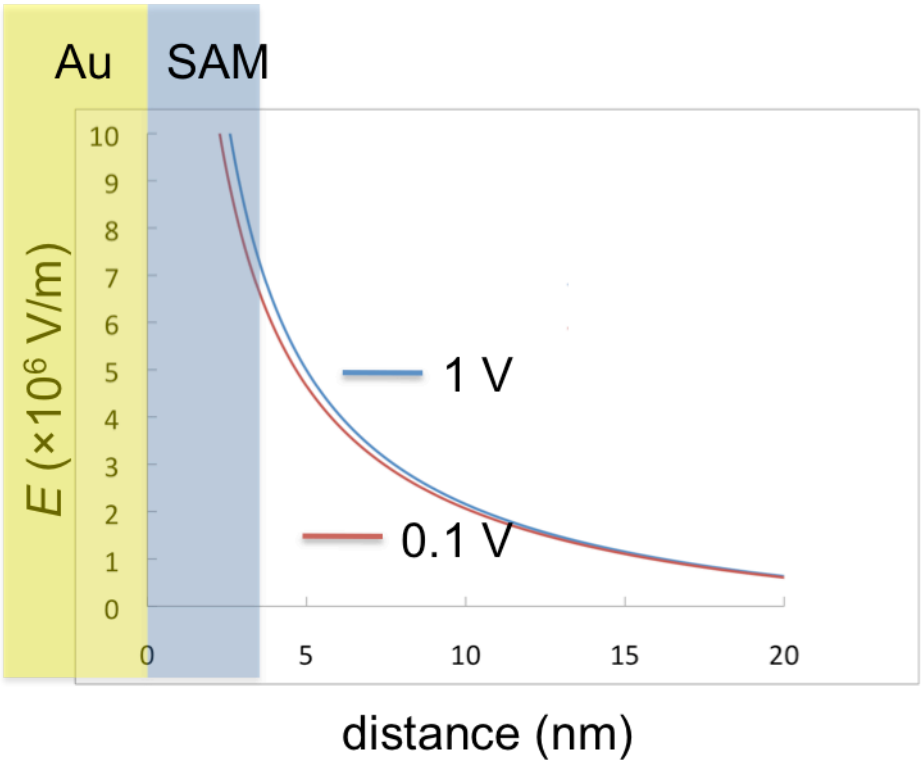

Figure 5.2. Electric field as a function of distance from the electrode. The electrode and the SAM are shown at the left side, with the surface of the Au set to 0 nm. The thickness of the SAM is about 3 nm.

We can see from Figure 5.2 that the electric field is completely screened within about 20 nm of the surface, which is less than the diameter of the microtubule (25 nm). If this accurately described our system, there would be no electrophoresis, showing that the precondition of equilibrium (and a Boltzmann particle distribution) is faulty. Thus, we expand our description to include the dynamics of the buffer ions, which, as shown in the next section returns a characteristic screening length that depends on the *undissociated* PIPES molecules.

5.2.2 Non-equilibrium: Screening, Ion Concentration and pH

Using the same assumptions as in the previous section (blocking electrodes, no electrolysis, 1-D system with PIPES the dominant ion), we show that the system is more accurately described by non-equilibrium phenomena such as current flow and dynamic local ion concentrations.

Initially, because PIPES has $\mathrm{p}K_\mathrm{a} = 6.8$ (the same value as the pH), half of the PIPES will be dissociated into $PIPES^{2-}$ as can be seen from:

$$\mathrm{pH} = \mathrm{p}K_\mathrm{a} - \log_{10}\frac{[\mathrm{PIPES}]}{[\mathrm{PIPES}^{2-}]}. \tag{5.4}$$

Thus, the major species in the PIPES buffer are: un-ionized PIPES, $PIPES^{2-}$ and H^+.

Under the electric field, ionic flux results in ion depletion of the central regions of the chamber. If we assume that locally, the solution is in equilibrium, PIPES, which is a weak acid, will be present along with $PIPES^{2-}$ and H^+. Le Chatelier's principle describes the effect of altering this equilibrium:

$$\mathrm{PIPES} \Leftrightarrow \mathrm{PIPES}^{2-} + 2\mathrm{H}^+. \tag{5.5}$$

If there are excess hydrogen ions, the equation will move to the left. If there is excess PIPES, more will dissociate, moving the equilibrium to the right. In our system, the induced ion flux will remove ions from the bulk, and cause PIPES to dissociate until either there is none remaining, or the electric field is fully screened by condensation of the ions at the electrodes, and migration of the ions ceases.

A more accurate estimation of the screening length than that given in the previous section would necessarily include the contribution from the reaction of PIPES.

Interestingly, this type of system has been analyzed for ion transport in a solid.[154] Although a full treatment is beyond the scope of this work, we can see a different characteristic length of the E-field screening when reactions are included:

$$L = \left(4\lambda \left(\frac{1}{\alpha_+} + \frac{1}{\alpha_-} + \frac{1}{\alpha_{\text{mol}}} \right) \right), \tag{5.6}$$

Where λ is a reaction rate coefficient, and the diffusion $D_i = \alpha_i \frac{\partial \mu_i}{\partial n_i}$ defines the α terms.

The final term in Equation 5.6 shows that there is a contribution from the undissociated PIPES, which is reasonable because the dissociation of PIPES will be affected by the flux of ions to the electrodes, as discussed in the previous section. Calculation of the actual value would require knowledge of the chemical potentials for each component. Nevertheless, we can see that whereas the equilibrium description fails to explain the behavior of the system, Equation 5.6 provides a broader view that does not assume a static concentration of ions by including reactions.

5.2.3 Implications for the Stability of MTs

From experiments in our laboratory, we have seen that the MTs are unstable (i.e. readily depolymerize) below about pH 6.0, indicating that bulk depletion of buffer ions, which maintain pH, could have negative side effects. In other words, due to the buffering action of PIPES, the pH will remain stable as long as PIPES is present in solution.[155] If however, all of the PIPES becomes dissociated and removed from the bulk to the

electrodes, the remaining solution will become sensitive to local pH changes that could lead to MT instability.

5.2.4 Minimum Force and Current for Deterministic Motion

It is well known that upon application of a potential to an electrolytic capacitor, the ions in the electrolyte quickly migrate to the capacitor plates with a speed dependent on the mobility of each ionic species. The finite amount of ions available to carry this current causes it to decay. At this point it is tempting to postulate that a current decay is at the root of the transience in our MT migration. Thus, we carried out simple 'four wire' I-V measurements to determine the electrical character of our flow chamber. The details of the measurements are included in Appendix E. The results show that the current decays to nanoampere values in a fraction of a second, below the detection limit of the test setup. This time is several orders of magnitude shorter than the time scale of the MT migration under the same conditions. Nevertheless, we cannot rule out the possibility that a minute current, which is below the detection limit of our four-wire measurement, is enough to drive MT migration. This raises the question: what is the minimum current required for inducing observable MT migration? We show here that a minimum value is on the order of ~100 nA.

Arguments put forth in previous works loosely define a distance for deterministic motion to be three times the standard deviation of the thermal diffusion distance in one dimension.[152,156,157] To put it another way, using this definition, if a particle moves a distance beyond that moved by randomly diffusing particles, then it is likely to be

undergoing deterministic motion due to the applied force. It is well known that a particle diffusing in a one dimensional random walk moves a distance x in a time *dt* according to

$$\left\langle |x|^2 \right\rangle = 2D\Delta t \tag{5.7}$$

where D is the diffusion coefficient. Also, because $\langle x \rangle = 0$, the variance of x is

$$\sigma = \sqrt{\left\langle x^2 \right\rangle - \langle x \rangle^2} = \sqrt{2D\Delta t} \tag{5.8}$$

We estimate the minimum force in the absence of retarding or relaxation forces to be

$$|F| = \gamma v = \gamma \frac{dx}{dt} \approx \gamma \frac{\Delta x}{\Delta t} \tag{5.9}$$

after Green, et al.[156] Omission of the relaxation force causes a slight underestimation of the minimum required force, so we will treat this value as the lower limit, below which no migration is possible. Using Einstein's relation that

$$D = \frac{k_B T}{\gamma}, \tag{5.10}$$

we use our definition of the migration distance to find the force in terms of known variables:

$$\Delta x = 3\sigma, \tag{5.11}$$

and

$$|F| = \sqrt{\frac{18 k_B T \gamma}{\Delta t}}, \tag{5.12}$$

where

$$\gamma_{\text{cylinder}} = \frac{4\pi\eta}{\ln(L/2r) + 0.84} \tag{5.13}$$

is the drag on a cylinder moving in the perpendicular direction, η is the viscosity of the PIPES buffer, L is the MT length and r is the MT radius.[1] Thus, for a 10 μm MT (25 nm in diameter, with η = 0.91 mPa s), under observation for 10 s, the minimum force to notice observable motion would be ~ 3 pN.[158] We can then use Equation 5.1 to estimate the current that this force corresponds to

$$F = QE = Q\rho j = \frac{Q\rho I}{A}; \tag{5.14}$$

or, in terms of current:

$$I = \frac{FA}{\rho Q}, \tag{5.15}$$

where ρ is the conductivity of the buffer (1.43 Vm A^{-1}), and A is the cross sectional area of the current path. We calculate Q from the length of the microtubule (10 μm), and its charge per unit length (conductivity and MT charge of -23 e/dimer from van den Heuvel, et al.).[135] This results in an estimated minimum current of ~100 nA, which is near the detection limit of our simple electrical characterization measurement. As a reference point, van den Heuvel, et al. were able to induce MT migration at a similar velocity to that seen in our work using constant applied currents around 140 nA in a capillary electrophoresis arrangement.[135]

5.2.5 Using the MT Migration Velocity to Measure Electric Field

In the previous section, we estimated the minimum force to produce MT migration as well as the lower limit of the force for a given current. Here we instead use the MT migration velocity to estimate the electric field in the chamber. We can use published values of the mobility and an estimate of the microtubule migration velocity to calculate the magnitude of the electric field using Equation 5.2 ($v = \mu E$). From van den Heuvel, who achieved the highest accuracy for measuring the mobility of MTs thus far, we average the perpendicular and parallel mobilities to arrive at: 2.37×10^{-8} m^2 $V^{-1}s^{-1}$. If we then estimate that the MTs move up to 60 microns (the height of the chamber) in about 100 s (see Figure 5.1), then the field would be 3×10^3 V cm^{-1}. This value is about 2 orders of magnitude lower than what we would have in a parallel plate capacitor at the same potential in vacuum (0.5 V across 60 microns), which makes our estimate of the E-field magnitude quite reasonable as the field is reduced significantly due to the ion polarization.

5.2.6 Alternate Explanations for the Decay in MT Migration

Because we cannot ascribe the decay in MT migration to the decay in current, then we must explain it through other mechanisms, of which several are possible and even likely. The most obvious is that the number of available MTs is finite, and is reduced as more and more move to the electrodes. Another possibility is that when the ions redistribute under the force of the imposed potential, a local pH change occurs that depolymerizes some MTs, as discussed in section 5.2.3. In this way, it is possible for MTs that are

farther away from the attracting pattern electrode to depolymerize before they are able to migrate into the stable area near the electrode. The depolymerization of MTs at pH of 5.5-6.0 was seen in our own laboratory in separate experiments.

5.2.7 Electrode Polarization

There are two reasons for the potentials lower than 0.5 V failing to induce MT migration. The first is that electrode polarization occurs spontaneously upon introducing an ion-containing buffer near conduction electrodes.[107] It is quite possible that a potential of a few hundred millivolts naturally accrues on the electrodes. In a second, related effect, the geometry of the flow cell may also contribute to the threshold potential. Namely, the current density will be higher above the center of the microelectrode than near the edges. Thus, for example, if one were to decrease the potential from 1 V, the size of the region that is above the threshold current is reduced, causing less and less MTs to be within the migration region.

5.3 Conclusion

We have shown that the ion current in the system decays quickly to ~ nA values, but that some current must remain in the chamber. This was proven by calculating the electric field at equilibrium using the Poisson-Boltzmann ion distribution and showing that the E-field is screened out within 20 nm of the surface. Through a calculation of the minimum force to achieve deterministic migration of MTs in the face of randomizing thermal forces, we determined that currents on the order of 100 nA are all that is required to drive the MT migration.

Ultimately to achieve higher levels of control over MTs in solution, one would control the electric field and thus the electrophoretic force directly. However, we have shown that complex ion migration responds to the field, making such direct control difficult. In the end improvements may be attained by incorporating real-time measurement of the current in the flow chamber with computer control over the applied potential, thus using continuous feedback to manipulate the current and MTs.

CHAPTER VI

OUTLOOK AND FUTURE WORK

6.1 Outlook

The incomplete understanding of the myriad roles of MTs in normal cellular function much less cancer and neurodegenerative diseases assures that these areas of research will remain highly active for years to come. In Alzheimer's disease, kinesin based transport along MTs is disrupted, impeding delivery of cellular material to the distal growing ends of nerve cells and ultimately causing loss of synaptic function and cell death.[17] Furthermore, the inability of nerves to regenerate has inspired materials scientists and neurobiologists to collaborate to treat the causes of paralysis and nerve damage.[159] More immediately related to the work in this dissertation, are the hurdles yet remaining for fabrication of fully operational MT-motor based devices and the wealth of opportunities in bio-synthetic interfaces which will maintain the high level of interest in these areas as well.[19] This section briefly reviews the path of the research in these areas in the near future.

Ultra high-resolution electron microscopes and AFMs are being turned to image the MT structure and motor decorated MTs.[160-165] Recent work with both contact and tapping mode AFM in solution has captured MT polymerization *in situ* and deformed MTs with pN forces for probing the elasticity.[166,167] Furthermore, the emerging method of combining fluorescence microscopy with AFM makes possible the study of both morphology and function of living cells in 3-D.[168]

In recent years, advances in molecular modeling of proteins has allowed simulation of MTs and tubulin in idealized environments for study of fundamental properties such as dielectric constant and bond strength, as well polymerization mechanisms.[169-173] Currently, due to the large number of molecules, no simulations using the entire MT exist, however, as computing power improves, simulations of the force generation and locomotion of kinesin motors will perhaps expand to include MT interactions.[174]

In cellular and structural biology, the area of microtubule-associated proteins, or MAPS, is very active. In recent years for instance, a variety of MAPs have been discovered which coordinate microtubule assembly, disassembly, cross-linking with the actin cytoskeleton, nucleation, and stabilization.[175,176] The further characterization and purification of these MAPs for use *in vitro* may serve as a tool for controlling MTs in a manner complementary to the work in this dissertation (further discussed in Future Work below).

As demonstrated in this paper, the low interaction of the MT with the surface allows for reversible adsorption of MTs, which is a prerequisite for ordered self-assembly and crystal growth.[139] This inspires the possibility for inducing assembly of MTs into ordered systems without additional MAPs or synthetic crosslinkers. Proposed experiments are discussed in more detail in Future Work below. Recent work by Sarveswaran, et al. demonstrated that a silane could be deposited from aqueous solution, allowing EBL patterned PMMA to be used as a mask for SAM patterning.[118] Furthermore, better methods for engineering biosynthetic interfaces are continuously

produced. For instance, new silanes which form antifouling SAMs with long-term stability will affect everything from medical implant technology to food packaging.[94]

6.2 Future Work

6.2.1 Nanoelectromechanical Systems for Controlling MT Polymerization

It is conceivable that one could fabricate polarly oriented MT tracks through controlling polymerization at the bio-synthetic interface (Figure 6.1). This would be done using the unpassivated style of pattern presented in chapter 4. First, short 'seed' MTs would be immobilized on the gold structure. Next, unpolymerized tubulin would be introduced into the flow chamber at a concentration below the critical concentration required for initiating MT growth. Then we would induce MT polymerization by locally concentrating the tubulin using electrophoresis, so that near the patterned surface, the tubulin would reach the critical concentration and extend the seed MTs in the direction of the pattern.

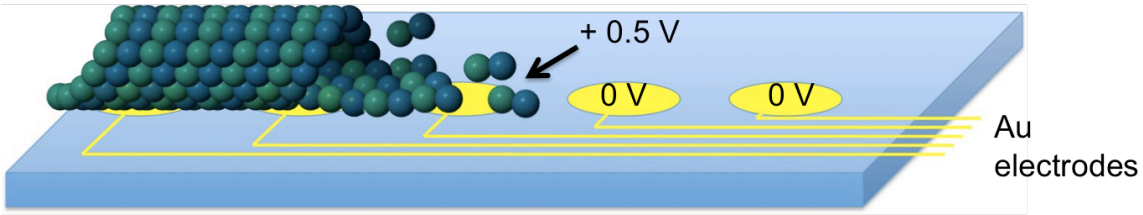

Figure 6.1. Inducing MT polymerization. The SAM prevents tubulin fouling while the electrodes induce local polymerization. The insulating glass substrate allows variation of the local potential by the nanoelectrodes.

Because the bulk tubulin concentration is too low to allow spontaneous MT growth, there will be no MT polymerization elsewhere in the chamber.[18] A modification of this approach would be using γ-tubulin, which is a microtubule nucleator instead of short MT 'seeds'.[147]

Polymerization *in situ* will allow us to control MT orientation from the outset, without having to orient preformed MTs externally or by surface binding, both of which have proven difficult.[107,149] Furthermore, this method is conducive to creating tracks and other patterns as MTs may be induced to grow in a unidirectional manner using lithographic patterns to localize the polymerization.

6.2.2 A Synthesized Axon?

The axon is the highly extended portion of nerve cells that extends to contact neighboring cells, forming a network of connections throughout the human body. Axons are mostly composed of microtubules and actin cytoskeletal filaments and act as pathways for the transport of intracellular cargo from the cell's core to its distal ends. A biomimetic (synthesized) axon would simulate a real axon but in a less complex, and more readily controlled cell-free environment.

As of the time of this work, there have been no reports of any type of engineered microtubule-based superstructures. Such a structure would require the nonfouling surfaces and oriented MT growth discussed above, but would also require controlling multiple MT interactions to bundle the MTs into the larger axon.[177,178] This may be possible using either the electrophoretic control outlined in this work, or by using the

cell's own machinery: the microtubule associated proteins.[179] Further, to maintain protein function outside the natural cellular environment, stricter environmental constraints would need to be implemented than used in this work. This would require one to keep the system stable for longer periods of time to allow multiple steps to be executed. This could be done using microfluidic channels both to mimic the geometric confinement of the cell membrane and to deliver tubulin and MAPs to the proper locations.

CHAPTER VII

SUMMARY

After analyzing several methods for passivation of glass and silicon surfaces to MT adsorption including hydrophilization, surfactants, PEG-SAMs and casein, we concluded that the organosilane PEG-SAMs exhibited the most desirable qualities: highly MT-resistant, compatible with EBL, and facilely prepared. The one-step SAM preparation method, which used a commercially available PEG-silane was presented in detail. This SAM prevented over 99 % of MT adsorption as compared to clean glass. Characterization of the SAM using ellipsometry, ARXPS and AFM, allowed us to estimate the surface density of the silane molecules and thus the orientation of the molecules in the monolayer. This characterization, in conjunction with the literature in the field of silane SAM formation, allowed us to propose a mechanism behind this MT-resistant behavior. This mechanism was based on a high density of cross-linked MPEOPS molecules that present low interacting methoxy groups at the solution interface. These results on the interaction of protein filaments with nonfouling SAMs complements previous studies which used smaller, globular proteins.[91]

The robust nonfouling SAM was successfully integrated with electron beam lithography for controlling *in vitro* MT-surface interactions. We determined that the SAM retained its passivating properties after lithographic patterning. Alternatively, when the SAM overlaid the lithographic patterns, forming a passivated electrode, we were able to produce on-demand, reversible MT trapping. Furthermore, single filaments

were shown to orient in a parallel fashion onto template electrodes in the form of gold lines and circles 1 micron in width, although the control over MT polarity remains a goal for future work.

We presented a new method for patterning SAMs which uses standard EBL to pattern *on* the SAM as opposed to more laborious methods which focus on controlling the location of the SAM molecules themselves.[38] For both the unpassivated and passivated patterns, the size and geometry of the gold patterns were limited only by the capabilities of the EBL system, with the smallest attainable features currently at about 10 nm, the same scale as single proteins.

We presented a simple overview of the forces at work during the directed assembly of MTs on the patterned surfaces. We concluded that after an initial fast current decay, a residual current on the order of 100 nA must be present to induce MT migration. We showed that an equilibrium description does not fit the system, and that current flow and buffer dissociation must be included in a full analysis. We also discussed reasons for the decay in MT migration over time as well as methods for improving the control of MT migration.

This method bridges the gap between nanoscale and mesoscale assembly of biomacromolecules on synthetic surfaces and is applicable to studies ranging from intracellular transport to biosensor technology. Because, like MTs, most proteins carry a native charge, the electrophoretic technique may be used for patterning many different proteins. Additionally, methods for crosslinking biomolecules to alkanethiol SAMs on gold are well developed and are capable of presenting a variety of functional surface

groups on the unpassivated gold pattern.[132] In order to assemble MT structures that mimic those found in cells, further work must be carried out to control MT-MT interactions and orient the MTs in an isopolar fashion. This may be possible through integration of kinesin motors and other microtubule associated proteins with the on-demand patterning and manipulation techniques presented here; ultimately providing a foundation for cell-free assembly of MT based superstructures.[19]

REFERENCES

1. Howard, J. *Mechanics of Motor Proteins and the Cytoskeleton*; Sinauer Associates: Sunderland, MA, 2001.
2. Vale, R. D.; Funatsu, T.; Pierce, D. W.; Romberg, L.; Harada, Y.; Yanagida, T. *Nature* **1996**, *380*, 451.
3. Goldstein, L. S. B.; Yang, Z. H. *Annu. Rev. Neurosci.* **2000**, *23*, 39.
4. Sawin, K. E.; Leguellec, K.; Philippe, M.; Mitchison, T. J. *Nature* **1992**, *359*, 540.
5. Rodriguez, O. C.; Schaefer, A. W.; Mandato, C. A.; Forscher, P.; Bement, W. M.; Waterman-Storer, C. M. *Nat. Cell Biol.* **2003**, *5*, 599.
6. Mitchison, T.; Kirschner, M. *Nature* **1984**, *312*, 237.
7. Seeman, N. C.; Belcher, A. M. *Proc. Natl. Acad. Sci. U. S. A.* **2002**, *99*, 6451.
8. Hyman, A. A. *J. Cell Sci.* **1991**, 125.
9. Diaz, J. F.; Valpuesta, J. M.; Chacon, P.; Diakun, G.; Andreu, J. M. *J. Biol. Chem.* **1998**, *273*, 33803.
10. Schiff, P. B.; Fant, J.; Horwitz, S. B. *Nature* **1979**, *277*, 665.
11. Shelanski, M. L.; Gaskin, F.; Cantor, C. R. *Proc. Natl. Acad. Sci. U. S. A.* **1973**, *70*, 765.
12. Hyman, A. A.; Chretien, D.; Arnal, I.; Wade, R. H. *J. Cell Biol.* **1995**, *128*, 117.
13. Wade, R. H.; Hyman, A. A. *Curr. Opin. Cell Biol.* **1997**, *9*, 12.
14. Gaskin, F.; Kress, Y. *J. Biol. Chem.* **1977**, *252*, 6918.

15. Phelps, K. K.; Walker, R. A. *Biochemistry* **2000**, *39*, 3877.

16. Santarella, R. A.; Skiniotis, G.; Goldie, K. N.; Tittmann, P.; Gross, H.; Mandelkow, E. M.; Mandelkow, E.; Hoenger, A. *J. Mol. Biol.* **2004**, *339*, 539.

17. Guzik, B. W.; Goldstein, L. S. *Curr. Opin. Cell Biol.* **2004**, *16*, 443.

18. Brown, T. B.; Hancock, W. O. *Nano Lett.* **2002**, *2*, 1131.

19. van den Heuvel, M. G. L.; Dekker, C. *Science* **2007**, *317*, 333.

20. Behrens, S.; Habicht, W.; Wu, J.; Unger, E. *Surf. Interface Anal.* **2006**, *38*, 1014.

21. Yebra, D. M.; Kiil, S.; Dam-Johansen, K. *Prog. Org. Coat.* **2004**, *50*, 75.

22. Le-Clech, P.; Chen, V.; Fane, T. A. G. *J. Membr. Sci.* **2006**, *284*, 17.

23. Kasemo, B. *Surf. Sci.* **2002**, *500*, 656.

24. Hlady, V.; Buijs, J. *Curr. Opin. Biotechnol.* **1996**, *7*, 72.

25. Gray, J. J. *Curr. Opin. Struct. Biol.* **2004**, *14*, 110.

26. Ostuni, E.; Chapman, R. G.; Holmlin, R. E.; Takayama, S.; Whitesides, G. M. *Langmuir* **2001**, *17*, 5605.

27. Wang, P.; Hill, T. G.; Wartchow, C. A.; Huston, M. E.; Oehler, L. M.; Smith, M. B.; Bednarski, M. D.; Callstrom, M. R. *J. Am. Chem. Soc.* **1992**, *114*, 378.

28. Perrino, C.; Lee, S.; Choi, S. W.; Maruyama, A.; Spencer, N. D. *Langmuir* **2008**, *24*, 8850.

29. Ulman, A. *Chem. Rev.* **1996**, *96*, 1533.

30. Prime, K. L.; Whitesides, G. M. *J. Am. Chem. Soc.* **1993**, *115*, 10714.

31. Xia, N.; Hu, Y. H.; Grainger, D. W.; Castner, D. G. *Langmuir* **2002**, *18*, 3255.

32. Branch, D. W.; Wheeler, B. C.; Brewer, G. J.; Leckband, D. E. *Biomaterials* **2001**, *22*, 1035.

33. Sharma, S.; Johnson, R. W.; Desai, T. A. *Langmuir* **2004**, *20*, 348.

34. Park, S. J.; Lee, K. B.; Choi, I. S.; Langer, R.; Jon, S. Y. *Langmuir* **2007**, *23*, 10902.

35. Cerruti, M.; Fissolo, S.; Carraro, C.; Ricciardi, C.; Majumdar, A.; Maboudian, R. *Langmuir* **2008**, *24*, 10646.

36. Emoto, K.; Van Alstine, J. M.; Harris, J. M. *Langmuir* **1998**, *14*, 2722.

37. Cecchet, F.; De Meersman, B.; Demoustier-Champagne, S.; Nysten, B.; Jonas, A. M. *Langmuir* **2006**, *22*, 1173.

38. Smith, R. K.; Lewis, P. A.; Weiss, P. S. *Prog. Surf. Sci.* **2004**, *75*, 1.

39. Horne, D. S. *Curr. Opin. Colloid Interface Sci.* **2002**, *7*, 456.

40. Bekos, E. J.; Ranieri, J. P.; Aebischer, P.; Gardella, J. A.; Bright, F. V. *Langmuir* **1995**, *11*, 984.

41. Turner, D. C.; Chang, C. Y.; Fang, K.; Brandow, S. L.; Murphy, D. B. *Biophysical Journal* **1995**, *69*, 2782.

42. Herrwerth, S.; Eck, W.; Reinhardt, S.; Grunze, M. *J. Am. Chem. Soc.* **2003**, *125*, 9359.

43. Boxshall, K.; Wu, M. H.; Cui, Z.; Cui, Z. F.; Watts, J. F.; Baker, M. A. *Surf. Interface Anal.* **2006**, *38*, 198.

44. Ho, C. H.; Limberis, L.; Caldwell, K. D.; Stewart, R. J. *Langmuir* **1998**, *14*, 3889.

45. Zhang, M. Q.; Ferrari, M. *Biotechnol. Bioeng.* **1997**, *56*, 618.

46. Harder, P.; Grunze, M.; Dahint, R.; Whitesides, G. M.; Laibinis, P. E. *J. Phys. Chem. B* **1998**, *102*, 426.

47. Sharma, S.; Desai, T. A. *J. Nanosci. Nanotechnol.* **2005**, *5*, 235.

48. Schreiber, F. *Prog. Surf. Sci.* **2000**, *65*, 151.

49. Mrksich, M.; Sigal, G. B.; Whitesides, G. M. *Langmuir* **1995**, *11*, 4383.

50. Li, L. Y.; Chen, S. F.; Zheng, J.; Ratner, B. D.; Jiang, S. Y. *J. Phys. Chem. B* **2005**, *109*, 2934.

51. Chen, S. F.; Liu, L. Y.; Jiang, S. Y. *Langmuir* **2006**, *22*, 2418.

52. Mrksich, M.; Whitesides, G. M. *Annu. Rev. Biophys. Biomol. Struct.* **1996**, *25*, 55.

53. Clare, T. L.; Clare, B. H.; Nichols, B. M.; Abbott, N. L.; Hamers, R. J. *Langmuir* **2005**, *21*, 6344.

54. Silin, V.; Weetall, H.; Vanderah, D. J. *J. Colloid Interface Sci.* **1997**, *185*, 94.

55. Dennis, J. R.; Howard, J.; Vogel, V. *Nanotechnology* **1999**, *10*, 232.

56. Aswal, D. K.; Lenfant, S.; Guerin, D.; Yakhmi, J. V.; Vuillaume, D. *Anal. Chim. Acta* **2006**, *568*, 84.

57. Verma, V.; Hancock, W. O.; Catchmark, J. M. *IEEE Trans. Adv. Packag.* **2005**, *28*, 584.

58. Fischer, T.; Hess, H. *J. Mater. Chem.* **2007**, *17*, 943.

59. van den Heuvel, M. G. L.; Butcher, C. T.; Smeets, R. M. M.; Diez, S.; Dekker, C. *Nano Lett.* **2005**, *5*, 1117.

60. van den Heuvel, M. G. L.; Butcher, C. T.; Lemay, S. G.; Diez, S.; Dekker, C. *Nano Lett.* **2005**, *5*, 235.

61. Papra, A.; Gadegaard, N.; Larsen, N. B. *Langmuir* **2001**, *17*, 1457.

62. Finocchio, E.; Macis, E.; Raiteri, R.; Busca, G. *Langmuir* **2007**, *23*, 2505.

63. Schwartz, D. K. *Annu. Rev. Phys. Chem.* **2001**, *52*, 107.

64. Lahiri, J.; Isaacs, L.; Tien, J.; Whitesides, G. M. *Anal. Chem.* **1999**, *71*, 777.

65. Zhu, X. Y.; Jun, Y.; Staarup, D. R.; Major, R. C.; Danielson, S.; Boiadjiev, V.; Gladfelter, W. L.; Bunker, B. C.; Guo, A. *Langmuir* **2001**, *17*, 7798.

66. Yang, Z. H.; Galloway, J. A.; Yu, H. U. *Langmuir* **1999**, *15*, 8405.

67. Malmsten, M.; Emoto, K.; Van Alstine, J. M. *J. Colloid Interface Sci.* **1998**, *202*, 507.

68. Zhang, M. Q.; Desai, T.; Ferrari, M. *Biomaterials* **1998**, *19*, 953.

69. Ma, H. W.; Hyun, J. H.; Stiller, P.; Chilkoti, A. *Adv. Mater.* **2004**, *16*, 338.

70. Shirahata, N.; Hozumi, A. *J. Nanosci. Nanotechnol.* **2006**, *6*, 1695.

71. Dekeyser, C. M.; Buron, C. C.; Mc Evoy, K.; Dupont-Gillain, C. C.; Marchand-Brynaert, J.; Jonas, A. M.; Rouxhet, P. G. *J. Colloid Interface Sci.* **2008**, *324*, 118.

72. Fadley, C. S. *Prog. Surf. Sci.* **1984**, *16*, 275.

73. McCrackin, F. L.; Passaglia, E.; Stromberg, R. R.; Steinber.Hl. *Journal of Research of the National Bureau of Standards Section a-Physics and Chemistry* **1963**, *A 67*, 363.

74. Norrman, K.; Papra, A.; Kamounah, F. S.; Gadegaard, N.; Larsen, N. B. *J. Mass Spectrom.* **2002**, *37*, 699.

75. Pale-Grosdemange, C.; Simon, E. S.; Prime, K. L.; Whitesides, G. M. *J. Am. Chem. Soc.* **1991**, *113*, 12.

76. Wallart, X.; de Villeneuve, C. H.; Allongue, P. *J. Am. Chem. Soc.* **2005**, *127*, 7871.

77. Popat, K. C.; Sharma, S.; Desai, T. A. *J. Phys. Chem. B* **2004**, *108*, 5185.

78. Powell, C. J.; Jablonski, A. *Nist Electron Effective-Attenuation-Length Database - Version 1.1*; National Institute of Standards and Technology: Gaithersburg, MD, 2003.

79. Sharma, S.; Johnson, R. W.; Desai, T. A. *Biosens. Bioelectron.* **2004**, *20*, 227.

80. Unsworth, L. D.; Sheardown, H.; Brash, J. L. *Langmuir* **2008**, *24*, 1924.

81. Brittain, W. J.; Minko, S. *J. Polym. Sci., Part A: Polym. Chem.* **2007**, *45*, 3505.

82. Zhuravlev, L. T. *Langmuir* **1987**, *3*, 316.

83. Bierbaum, K.; Kinzler, M.; Woll, C.; Grunze, M.; Hahner, G.; Heid, S.; Effenberger, F. *Langmuir* **1995**, *11*, 512.

84. van der Boom, M. E.; Evmenenko, G.; Yu, C. J.; Dutta, P.; Marks, T. J. *Langmuir* **2003**, *19*, 10531.

85. Brzoska, J. B.; Benazouz, I.; Rondelez, F. *Langmuir* **1994**, *10*, 4367.

86. Le Grange, J. D.; Markham, J. L.; Kurkjian, C. R. *Langmuir* **1993**, *9*, 1749.

87. Finklea, H. O.; Robinson, L. R.; Blackburn, A.; Richter, B.; Allara, D.; Bright, T. *Langmuir* **1986**, *2*, 239.

88. Krasnoslobodtsev, A. V.; Smirnov, S. N. *Langmuir* **2002**, *18*, 3181.

89. McGovern, M. E.; Kallury, K. M. R.; Thompson, M. *Langmuir* **1994**, *10*, 3607.

90. Unsworth, L. D.; Sheardown, H.; Brash, J. L. *Langmuir* **2005**, *21*, 1036.

91. Satulovsky, J.; Carignano, M. A.; Szleifer, I. *Proceedings of the National Academy of Sciences of the United States of America* **2000**, *97*, 9037.

92. Jeon, S. I.; Lee, J. H.; Andrade, J. D.; Degennes, P. G. *J. Colloid Interface Sci.* **1991**, *142*, 149.

93. Ariga, K.; Nakanishi, T.; Michinobu, T. *J. Nanosci. Nanotechnol.* **2006**, *6*, 2278.

94. Senaratne, W.; Andruzzi, L.; Ober, C. K. *Biomacromolecules* **2005**, *6*, 2427.

95. Ladd, J.; Boozer, C.; Yu, Q.; Chen, S.; Homola, J.; Jiang, S. *Langmuir* **2004**, *20*, 8090.

96. Bretagnol, F.; Valsesia, A.; Sasaki, T.; Ceccone, G.; Colpo, P.; Rossi, F. *Adv. Mater.* **2007**, *19*, 1947.

97. Kannan, B.; Castelino, K.; Chen, F. F.; Majumdar, A. *Biosens. Bioelectron.* **2006**, *21*, 1960.

98. Muthukrishnan, G.; Roberts, C. A.; Chen, Y. C.; Zahn, J. D.; Hancock, W. O. *Nano Lett.* **2004**, *4*, 2127.

99. Gittes, F.; Meyhofer, E.; Baek, S.; Howard, J. *Biophys. J.* **1996**, *70*, 418.

100. Doot, R. K.; Hess, H.; Vogel, V. *Soft Matter* **2007**, *3*, 349.

101. Yokokawa, R.; Yoshida, Y.; Takeuchi, S.; Kon, T.; Fujita, H. *Nanotechnology* **2006**, *17*, 289.

102. Lin, C. T.; Kao, M. T.; Kurabayashi, K.; Meyhofer, E. *Nano Lett.* **2008**, *8*, 1041.

103. Romet-Lemonne, G.; VanDuijn, M.; Dogterom, M. *Nano Lett.* **2005**, *5*, 2350.

104. Hiratsuka, Y.; Tada, T.; Oiwa, K.; Kanayama, T.; Uyeda, T. Q. P. *Biophys. J.* **2001**, *81*, 1555.

105. Cohen, A. E. *Phys. Rev. Lett.* **2005**, *94*.

106. Cole, M. A.; Voelcker, N. H.; Thissen, H. *Smart Mater. Struct.* **2007**, *16*, 2222.

107. Minoura, I.; Muto, E. *Biophys. J.* **2006**, *90*, 3739.

108. Platt, M.; Muthukrishnan, G.; Hancock, W. O.; Williams, M. E. *J. Am. Chem. Soc.* **2005**, *127*, 15686.

109. Vassilev, P. M.; Dronzine, R. T.; Vassileva, M. P.; Georgiev, G. A. *Biosci. Rep.* **1982**, *2*, 1025.

110. Xia, Y. N.; Rogers, J. A.; Paul, K. E.; Whitesides, G. M. *Chem. Rev.* **1999**, *99*, 1823.

111. Kane, R. S.; Takayama, S.; Ostuni, E.; Ingber, D. E.; Whitesides, G. M. *Biomaterials* **1999**, *20*, 2363.

112. Jiang, J.; Li, X. M.; Mak, W. C.; Trau, D. *Adv. Mater.* **2008**, *20*, 1636.

113. Stamou, D.; Musil, C.; Ulrich, W. P.; Leufgen, K.; Padeste, C.; David, C.; Gobrecht, J.; Duschl, C.; Vogel, H. *Langmuir* **2004**, *20*, 3495.

114. Pallandre, A.; Glinel, K.; Jonas, A. M.; Nysten, B. *Nano Lett.* **2004**, *4*, 365.

115. Falconnet, D.; Koenig, A.; Assi, T.; Textor, M. *Adv. Funct. Mater.* **2004**, *14*, 749.

116. Denis, F. A.; Pallandre, A.; Nysten, B.; Jonas, A. M.; Dupont-Gillain, C. C. *Small* **2005**, *1*, 984.

117. Choi, K. H.; Bourgoin, J. P.; Auvray, S.; Esteve, D.; Duesberg, G. S.; Roth, S.; Burghard, M. *Surf. Sci.* **2000**, *462*, 195.

118. Sarveswaran, K.; Hu, W. C.; Huber, P. W.; Bernstein, G. H.; Lieberman, M. *Langmuir* **2006**, *22*, 11279.

119. Harnett, C. K.; Satyalakshmi, K. M.; Craighead, H. G. *Langmuir* **2001**, *17*, 178.

120. Behm, J. M.; Lykke, K. R.; Pellin, M. J.; Hemminger, J. C. *Langmuir* **1996**, *12*, 2121.

121. Rundqvist, J.; Hoh, J. H.; Haviland, D. B. *Langmuir* **2006**, *22*, 5100.

122. Tarlov, M. J.; Burgess, D. R. F.; Gillen, G. *J. Am. Chem. Soc.* **1993**, *115*, 5305.

123. Yin, H. B.; Brown, T.; Greef, R.; Wilkinson, J. S.; Melvin, T. *Microelectron. Eng.* **2004**, *73-4*, 830.

124. Hyun, J.; Ahn, S. J.; Lee, W. K.; Chilkoti, A.; Zauscher, S. *Nano Lett.* **2002**, *2*, 1203.

125. Hyun, J.; Chilkoti, A. *J. Am. Chem. Soc.* **2001**, *123*, 6943.

126. Ghosh, M.; Alves, C.; Tong, Z.; Tettey, K.; Konstantopoulos, K.; Stebe, K. J. *Langmuir* **2008**, *24*, 8134.

127. Zhao, J. W.; Uosaki, K. *Nano Lett.* **2002**, *2*, 137.

128. Franks, W.; Tosatti, S.; Heer, F.; Seif, P.; Textor, M.; Hierlemann, A. *Biosens. Bioelectron.* **2007**, *22*, 1426.

129. Kannan, B.; Kulkarni, R. P.; Majumdar, A. *Nano Lett.* **2004**, *4*, 1521.

130. Michel, R.; Reviakine, I.; Sutherland, D.; Fokas, C.; Csucs, G.; Danuser, G.; Spencer, N. D.; Textor, M. *Langmuir* **2002**, *18*, 8580.

131. Veiseh, M.; Wickes, B. T.; Castner, D. G.; Zhang, M. Q. *Biomaterials* **2004**, *25*, 3315.

132. Love, J. C.; Estroff, L. A.; Kriebel, J. K.; Nuzzo, R. G.; Whitesides, G. M. *Chem. Rev.* **2005**, *105*, 1103.

133. Sabatani, E.; Rubinstein, I.; Maoz, R.; Sagiv, J. *J. Electroanal. Chem.* **1987**, *219*, 365.

134. Wong, P. K.; Wang, T. H.; Deval, J. H.; Ho, C. M. *Ieee-Asme Transactions on Mechatronics* **2004**, *9*, 366.

135. van den Heuvel, M. G. L.; de Graaff, M. P.; Lemay, S. G.; Dekker, C. *Proc. Natl. Acad. Sci. U. S. A.* **2007**, *104*, 7770.

136. van den Heuvel, M. G. L.; Bondesan, R.; Lagomarsino, M. C.; Dekker, C. *Phys. Rev. Lett.* **2008**, *101*.

137. Bohm, K. J.; Mavromatos, N. E.; Michette, A.; Stracke, R.; Unger, E. *Electromagnetic Biology and Medicine* **2005**, *24*, 319.

138. Hunt, A. J.; Gittes, F.; Howard, J. *Biophys. J.* **1994**, *67*, 766.

139. Whitesides, G. M.; Boncheva, M. *Proc. Natl. Acad. Sci. U. S. A.* **2002**, *99*, 4769.

140. Desai, A.; Mitchison, T. J. *Annu. Rev. Cell Dev. Biol.* **1997**, *13*, 83.

141. Mitchison, T.; Kirschner, M. *Nature* **1984**, *312*, 232.

142. Dogterom, M.; Kerssemakers, J. W.; Romet-Lemonne, G.; Janson, M. E. *Curr. Opin. Cell Biol.* **2005**, *17*, 67.

143. Yang, Y.; Deymier, P. A.; Wang, L.; Guzman, R.; Hoying, J. B.; McLaughlin, H. J.; Smith, S. D.; Jongewaard, I. N. *Biotechnol. Progr.* **2006**, *22*, 303.

144. Huang, Y. M.; Uppalapati, M.; Hancock, W. O.; Jackson, T. N. *Biomed. Microdevices* **2007**, *9*, 175.

145. Yokokawa, R.; Murakami, T.; Sugie, T.; Kon, T. *Nanotechnology* **2008**, *19*.

146. Wiese, C.; Zheng, Y. X. *J. Cell Sci.* **2006**, *119*, 4143.

147. Spoerke, E. D.; Bachand, G. D.; Liu, J.; Sasaki, D.; Bunker, B. C. *Langmuir* **2008**, *24*, 7039.

148. Bohm, K. J.; Stracke, R.; Muhlig, P.; Unger, E. *Nanotechnology* **2001**, *12*, 238.

149. Limberis, L.; Magda, J. J.; Stewart, R. J. *Nano Lett.* **2001**, *1*, 277.

150. Hutchins, B. M.; Hancock, W. O.; Williams, M. E. *PCCP* **2006**, *8*, 3507.

151. Hyman, A. A. In *Preparation of Marked Microtubules for the Assay of the Polarity of Microtubule-Based Motors by Fluorescence*, 1991; Company of Biologists Ltd: 1991; pp 125.

152. Green, N. G.; Ramos, A.; Morgan, H. *Journal of Physics D-Applied Physics* **2000**, *33*, 632.

153. Probstein, R. F. *Physicochemical Hydrodynamics: An Introduction*; Butterworths: Boston, Mass., 1989.

154. Saslow, W. M. *Physical Review B* **2004**, *70*.

155. Good, N. E.; Winget, G. D.; Winter, W.; Connolly, T. N.; Izawa, S.; Singh, R. M. M. *Biochemistry* **1966**, *5*, 467.

156. Green, N. G.; Ramos, A.; Morgan, H.; Castellanos, A. In *Sub-Micrometre Ac Electrokinetics: Particle Dynamics under the Influence of Dielectrophoresis and Electrohydrodynamics*, 1999; Taylor, D. M., Ed. 1999; pp 89.

157. Zheng, L. F.; Li, S. D.; Brody, J. P.; Burke, P. J. *Langmuir* **2004**, *20*, 8612.

158. Kim, T.; Kao, M. T.; Hasselbrink, E. F.; Meyhofer, E. *Biophys. J.* **2008**, *94*, 3880.

159. Panseri, S.; Cunha, C.; Lowery, J.; Del Carro, U.; Taraballi, F.; Amadio, S.; Vescovi, A.; Gelain, F. *BMC Biotechnol.* **2008**, *8*, 12.

160. Moores, C. *Introduction to Electron Microscopy for Biologists* **2008**, *88*, 299.

161. Qazi, U.; Niederstrasser, H.; Nogales, E. *Molecular Biology of the Cell* **2000**, *11*, 978.

162. Muller, S. A.; Aebi, U.; Engel, A. *J. Struct. Biol.* **2008**, *163*, 235.

163. Tan, D. Y.; Rice, W. J.; Sosa, H. *Structure* **2008**, *16*, 1732.

164. Zhou, D. X.; Jiang, X. D.; Xu, R. X.; Cai, Y. Q.; Hu, J. L.; Xu, G.; Zou, Y. X.; Zeng, Y. J. *Cell. Mol. Neurobiol.* **2008**, *28*, 895.

165. Kacher, C. M.; Weiss, I. M.; Stuart, R. J.; Schmidt, C. F.; Hansma, P. K.; Radmacher, M.; Fritz, M. *European Biophysics Journal with Biophysics Letters* **2000**, *28*, 611.

166. Kis, A.; Kasas, S.; Kulik, A. J.; Catsicas, S.; Forro, L. *Langmuir* **2008**, *24*, 6176.

167. Thomson, N. H.; Kasas, S.; Riederer, B. M.; Catsicas, S.; Dietler, G.; Kulik, A. J.; Forro, L. *Ultramicroscopy* **2003**, *97*, 239.

168. Kondra, S.; Laishram, J.; Ban, J.; Migliorini, E.; Di Foggia, V.; Lazzarino, M.; Torre, V.; Ruaro, M. E. *J. Neurosci. Methods* **2009**, *177*, 94.

169. Mershin, A.; Kolomenski, A. A.; Schuessler, H. A.; Nanopoulos, D. V. *BioSyst.* **2004**, *77*, 73.

170. Tuszynski, J. A.; Brown, J. A.; Crawford, E.; Carpenter, E. J.; Nip, M. L. A.; Dixon, J. M.; Sataric, M. V. *Mathematical and Computer Modelling* **2005**, *41*, 1055.

171. Drabik, P.; Gusarov, S.; Kovalenko, A. *Biophys. J.* **2007**, *92*, 394.

172. Dima, R. I.; Joshi, H. *Proc. Natl. Acad. Sci. U. S. A.* **2008**, *105*, 15743.

173. Neek-Amal, M.; Radja, N. H.; Ejtehadi, M. R. *Phys. Rev. E* **2008**, *78*, 9.

174. Hwang, W.; Lang, M. J.; Karplus, M. *Structure* **2008**, *16*, 62.

175. Mandelkow, E.; Mandelkow, E. M. *Curr. Opin. Cell Biol.* **1995**, *7*, 72.

176. Hoenger, A.; Gross, H., Structural Investigations into Microtubule-Map Complexes. In *Biophysical Tools for Biologists: Vol 1 in Vitro Techniques*, Elsevier Academic Press Inc: San Diego, 2008; Vol. 84, pp 425.

177. Myers, K. A.; He, Y.; Hasaka, T. R.; Baas, P. W. *Neuroscientist* **2006**, *12*, 107.

178. Needleman, D. J.; Ojeda-Lopez, M.; Raviv, U.; Ewert, K.; Jones, J.; Miller, H.; Wilson, L.; Safinya, C. R. In *Microtubule Bundling and Shape Transitions: Mechanics, Interactions, and Stabilization*, 2005; 2005; pp 644A.

179. Dehmelt, L.; Halpain, S. *J. Neurobiol.* **2004**, *58*, 18.

APPENDIX

A. Calculating Mass of MTs Adsorbed on SAM

The results for the amount of MTs fouled on the test surfaces are given above as adsorption normalized to a clean glass slide. To compare the amount of protein adsorbed to values published in other reports, we must convert this percent area to a measure of adsorbed mass. Because the mass of the tubulin dimer is known and the number of tubulin dimers in an MT can be estimated with reasonable accuracy, we simply need to determine the length of the MTs to find their mass. During the passivation assay, the total area covered by MTs was automatically measured by dividing the number of pixels above a given fluorescence intensity by the total area imaged. This area, A, should be directly proportional to the length of the adsorbed MTs, l, as they are all in the plane of the image.

$$A = lw,$$

where w is the effective width of the MTs. Thus, w is a proportionality constant that can be determined by measuring the length of some sample MTs, plotting the result versus the measured area, and fitting to a linear function. In this way, we obtain a reasonable value for w (and thus MT length) without manually measuring the length of thousands of MTs.

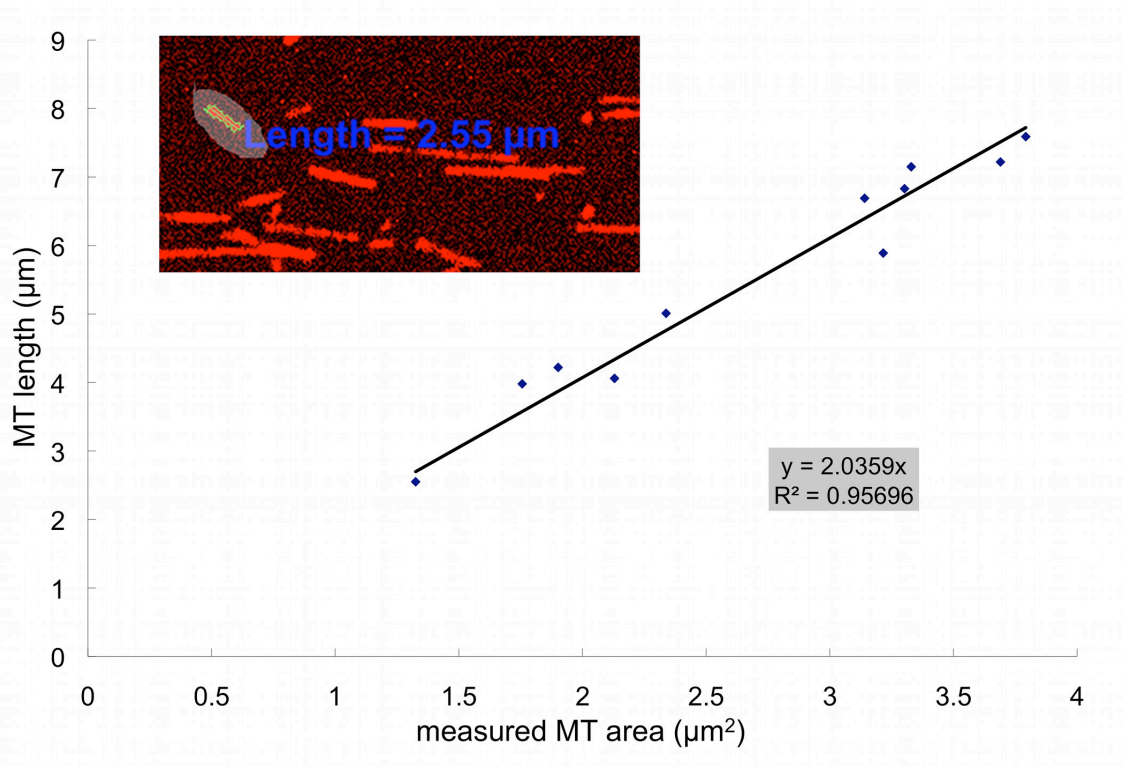

Figure A1. Measurement of MT length and plot of MT Area vs. length.

The number of dimers in an MT of given length can be estimated using the facts that most GMPCPP MTs have 14 protofilaments and that the dimer is 8 nm long. Once the MT length is known the mass may be calculated:

$$m = \lambda l,$$

where m is the MT mass and λ is the linear mass density of the MTs. Assuming that the MT is made up of 14 protofilaments, and the tubulin dimer has a mass of 110 kDa and length of 8 nm,

$$\lambda = 3.2 \times 10^{-7}\ \text{ng/µm}.$$ [1-3]

Using this conversion on the value for average MT adsorption found in the passivation assay returns the MT area per image. Dividing by the area imaged at 60X (9408 μm^2) gives us a total tubulin density of 2.4×10^7 ng/cm^2.

There are several sources of error from this method. The area covered by overlapping or crossed MTs was only counted once during the computer analysis. Further, only the middle range of MT lengths were calibrated against the area measurement, as it is difficult to measure the length of very long or short MTs. These problems are assumed to have a minimal effect on the mass calculation as most MTs were well separated and were of medium length. Additionally, this method assumes that all of the protofilaments in an MT had the same, well-defined end point. In practice, the ends of the MTs are likely somewhat ragged with some isolated dangling protofilaments, although the amount of tubulin in these ends is likely very small.

B. Polarity Marked MT Polymerization

To mark MTs polarly, N-ethylmaleimide was added to brightly labeled MT 'seeds' as below. Tubulin and rhodamine tubulin were reconstituted in PIPES buffer and stored at -80°C as discussed in chapter 2 of the main text. NEM tubulin was prepared by adding NEM at 1mM (prepared fresh in deionized water) before freezing and storing the tubulin. Brightly labeled seeds were prepared by adding unlabeled tubulin to labeled tubulin at a ratio of 2:1 and kept on ice. Immediately following, the NEM tubulin was then mixed with labeled and unlabeled tubulin at a ratio of 1:3:24 and incubated for 5 min on ice. Then this mixture was incubated at 37°C for 1 min before mixing in the

brightly labeled seeds. The latter are added at a volume of 1/10 of the NEM elongation mixture. This final mixture is incubated at 37°C for 20 minutes then suspended at 1/100 in PIPES buffer.

C. Observing Bulk Fluid Flow During Electrophoresis Using Microbeads

To determine that the migration of MTs was due to electrophoretic (Coulombic) migration, and not bulk fluid flow from electroosmosis or convection, we replaced the MTs in the flow chamber with charge neutral fluorescent polystyrene beads (Spherotech, Inc.). Because electroosmosis and convection are caused by the viscous drag from buffer migration and heating, respectively, they occur independently of the added molecules (MTs or microbeads). Thus, if these effects contributed to the migration of MTs, they would also cause microbead migration due to viscous drag of the fluid on the beads.

The procedure, except for the substitution of microbeads for MTs, was the same as outlined in the previous sections, from lithography (Section 4.2) to electrophoresis (Section 4.3).

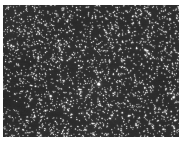

Figure C 1. Fluorescent microbeads in flow chamber. The microbeads diffuse through out the chamber and do not migrate upon application of the field.

Upon application of the field, we did not observe microbead migration during ~ 1 hr. observation period. Interestingly, the microbeads did foul on the SAM and passivated electrode, showing that the MT-antifouling SAM is not universally resistant to fouling.

D. Poisson-Boltzmann Calculation of Charge Distribution

We can calculate the electric field in the capacitor after equilibrium has been reached. From Poisson's equation, if we take the liberty to assume that the electrode is large, or limit the region of interest to the center of the electrode, we have for a linear dielectric medium:

$$\nabla^2\Phi \rightarrow \frac{d^2\Phi}{dy^2} = -\frac{\rho(\Phi)}{\varepsilon}, \tag{D.1}$$

where $\rho(\Phi) = \sum_i e n_i(\Phi) z_i$, Φ is the potential, n_i and n_i^0 are the number concentration for species *i*, with and without potential, respectively, *z* is the charge number, and *e* is the elementary charge.[4] By using the definition of the derivative, we can write Equation D.1 as

$$\frac{d^2\Phi}{dy^2} = \frac{1}{2}\frac{d}{d\Phi}\left(\frac{d\Phi}{dy}\right)^2 = -\frac{\rho(\Phi)}{\varepsilon}, \tag{D.2}$$

where ε is the permittivity of the medium.

Rearranging

$$d\left(\frac{d\Phi}{dy}\right)^2 = -\frac{2\rho(\Phi)}{\varepsilon}d\Phi \tag{D.3}$$

Integrating and rearranging gives:

$$\frac{d\Phi}{dy} = \left(-\int \frac{2\rho(\Phi)}{\varepsilon} d\Phi \right)^{1/2} = -E. \tag{D.4}$$

We then insert Equation D.3, evaluate the elementary integral, and evaluate it for potentials ranging from 0.001 V to 1.5 V, the real experimental values.

For an equilibrium distribution of indistinguishable particles, Boltzmann statistics holds and we can write the distribution of each species as

$$n_i(\Phi) = n_i^0 z_i e^{-\beta e z_i \Phi} \tag{D.5}$$

where $\beta = \frac{1}{k_B T}$,

and ρ is an implicit function of Φ:

$$\rho(\Phi) = e \sum_i n_i^0 z_i e^{-\beta e z_i \Phi}. \tag{D.6}$$

To evaluate the integral, we express the ion distribution as the difference between the position-dependent value and the bulk value at infinity[4]:

$$n_i(\Phi) = n_i(y) - n_i^\infty = n_i^\infty (z_i e^{-\beta e z_i \Phi} - 1) \tag{D.7}$$

For the values of the concentration we note that although the PIPES is added at 80mM (see Chapter 2 for buffer preparation), in the equilibrium state, only ½ of the PIPES molecules will be dissociated due to its dissociation constant of 6.8 (see section 5.2.2), while the magnesium chloride will be fully dissolved:

$$n_{\text{PIPES}}^\infty = 0.04 \text{ mol L}^{-1}$$
$$n_{\text{MgCl}_2}^\infty = 0.001 \text{ mol L}^{-1}$$

Because the pH of the buffer is adjusted to ~ 7 by KOH, we do not include the contribution from free H^+ and OH^- ions. The K^+ is also ignored, as the amount of KOH added is very low (about 100 μM). We use a temperature of 300 °K for all calculations, and a permittivity of $\varepsilon = 80.1\,\varepsilon_0$ for water.

E. Electrical Characterization of Flow Cell

We characterized the electrical properties of the flow cell by performing four wire I-V measurements. The same flow cell assembly procedure was used as outlined for the MT patterning experiments with the passivated electrode. The setup was composed of two precision digital multimeters (DMM) and a DC power supply connected to the assembled flow chamber just as in the electrophoresis experiments. The DMMs were connected to a computer running Labview, which simply recorded the current (DMM1) or voltage (DMM2) and the time for each measurement. Labview was configured to record the *I* and *V* values as quickly as possible, resulting in approximately three readings per second. Upon filling the chamber with PIPES buffer and applying DC potentials up to 1.5 V, the current in the flow chamber as a function of time was measured by recording the voltage across a series reference resistor.

1. Diaz, J. F.; Valpuesta, J. M.; Chacon, P.; Diakun, G.; Andreu, J. M. *J. Biol. Chem.* **1998**, *273*, 33803.
2. Vale, R. D.; Coppin, C. M.; Malik, F.; Kull, F. J.; Milligan, R. A. *J. Biol. Chem.* **1994**, *269*, 23769.
3. Hyman, A. A.; Chretien, D.; Arnal, I.; Wade, R. H. *J. Cell Biol.* **1995**, *128*, 117.
4. Probstein, R. F., *Physicochemical Hydrodynamics: An Introduction*. Butterworths: Boston, Mass., 1989; p 353.

VITA

Name: John A. Noel

Address: Physics Dept., Texas A&M University
College Station, TX 77843-4242

Email Address: jnoel@physics.tamu.edu

Education: B.S., Physics, Texas A&M University, 2003